Available online at www.sciencedirect.com

ScienceDirect

Comput. Methods Appl. Mech. Engrg. 388 (2022) 114189

Computer methods in applied mechanics and engineering

www.elsevier.com/locate/cma

On tailoring fracture resistance of brittle structures: A level set interface-enriched topology optimization approach

Jian Zhang, Fred van Keulen, Alejandro M. Aragón*

Faculty of Mechanical, Maritime and Materials Engineering, Delft University of Technology, Mekelweg 2, 2628 CD Delft, The Netherlands

Received 4 June 2021; received in revised form 10 September 2021; accepted 12 September 2021
Available online 19 October 2021

Graphical Abstract

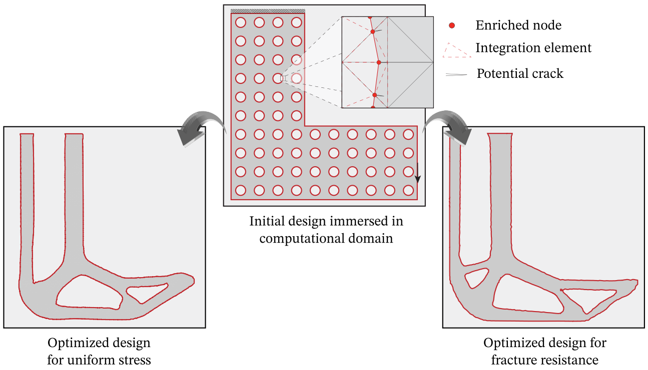

Abstract

We propose a fully immersed topology optimization procedure to design structures with tailored fracture resistance under linear elastic fracture mechanics assumptions for brittle materials. We use a level set function discretized by radial basis functions to represent the topology and the Interface-enriched Generalized Finite Element Method (IGFEM) to obtain an accurate structural response. The technique assumes that cracks can nucleate at right angles from the boundary, at the location of enriched nodes that are added to enhance the finite element approximation. Instead of performing multiple finite element analyses to evaluate the energy release rates (ERRs) of all potential cracks—a procedure that would be computationally intractable—we approximate them by means of topological derivatives after a *single* enriched finite element analysis of the *uncracked* domain. ERRs are then aggregated to construct the objective function, and the corresponding sensitivity formulation is derived analytically by means of an adjoint formulation. Several numerical examples demonstrate the technique's ability to tailor fracture resistance, including the well-known benchmark L-shaped bracket and a multiple-loading optimization problem for obtaining a structure with fracture resistance anisotropy.

---

* Corresponding author.
E-mail address: a.m.aragon@tudelft.nl (A.M. Aragón).

https://doi.org/10.1016/j.cma.2021.114189

Keywords: Topological derivatives; Level set; Stress recovery technique; Linear elastic fracture mechanics; Enriched finite element analysis; Interface-enriched generalized finite element method (IGFEM)

1. Introduction

Cracks in engineering structures, which could develop during their manufacturing or service life, may affect adversely the mechanical performance and even lead to catastrophic failure (particularly brittle fracture). When it is either impractical or just too expensive to simply change a defective component, a structure could be reconditioned by simply applying adhesively bonded patches [1–3]. Nevertheless, without any doubt the best way to mitigate the effect of cracks is preventing them from materializing in the first place. Structural failure due to fracture should therefore be considered in the early stages of structural design. At worst, the engineer should follow guidelines of best practices to avoid unsafe designs. At best, computational tools should be used to obtain designs that have been optimized to reduce the likelihood of fracture or other mechanisms that could compromise structural integrity. One such tool is topology optimization [4–7], which has become a popular design technique in real-world industrial applications [8,9]. Based on structural failure criteria, topology optimization procedures can be classified into three categories: stress-, damage-, and fracture-based approaches.

Stress-based topology optimization is by far the most widely used technique. In this procedure, the stress state in the final design must fulfill a stress requirement, for instance, not exceeding the yield strength. Therefore, yield criteria such as von Mises [10–13] and Drucker–Prager [14,15] are enforced as constraints. Moreover, various static failure theories for brittle and ductile materials have also been used in topology optimization [16]. Since stress is a local quantity, a large number of stress constraints must be satisfied, making the optimization complex and computationally demanding [17,18]. To circumvent this, one approach widely used is to employ aggregation functions that group all stress-based terms into a single quantity; aggregation functions include the Kreisselmeier–Steinhauser (KS) [19], P-mean [20], and P-norm [21]. As a caveat, although these stress measures simplify the computational implementation, they also “globalize” stress so local values are harder to enforce *exactly*. As a result, various techniques have been proposed to recover stress locality, including divide-and-conquer strategies, where aggregation functions are used on various disjoint subdomains [22,23], and stress fields that are weighted by the structural boundary’s curvature [24] (which significantly influences stress concentrations [25]). An alternative approach to the use of aggregation functions was recently proposed, whereby an augmented Lagrangian formulation is used to deal with a large number of local stress constraints in the objective function directly [26]. Instead of considering stresses as constraints, the stress distribution can also be directly minimized, for which the optimization requires a global stress measure [27–29].

Damage-based topology optimization has also gained considerable attention in the past decade. The idea, which was first explored by Bendsøe and Diaz [30], introduced damage-related criteria either as an objective or constraint. They used a continuum damage model to reinforce an existing structure for minimum damage. Another procedure based on continuum damage was later proposed to maximize the stiffness of concrete structures by optimizing the rebar layout [31]. Amir [32] then extended this method to design concrete structures with minimum weight, in which both the rebar and concrete layout were optimized simultaneously. James and Waisman [33] also used the above damage model to optimize structures with minimum weight under the constraint on maximum local damage. They later used their approach to solve multiple-loading optimization problems, where superposition was used to consider the influence of damage accumulation [34]. All these studies focused on continuum damage models for brittle materials. Elastoplastic damage models were also investigated for designing energy absorbing structures [35–37], where the objective was to maximize plastic work while constraining maximum damage.

As strength and fracture toughness are usually inversely proportional to each other in many materials [38], fracture criteria have also been explored in structural optimization. Works in this category can be classified according to whether cracks are *stationary* or *evolving* (allowed to nucleate and/or propagate). In the former category cracks are therefore predefined in the computational domain and topology optimization is used to mitigate their effect. Kang *et al.* [39] borrowed linear elastic fracture mechanics (LEFM) concepts and considered the energy release rate (ERR)—amount of energy available for crack extension—evaluated by means of the J-integral [40] in their optimization. In fact, they solved a multi-objective optimization problem, where structural compliance and ERRs were considered as separate objective functions optimized simultaneously, yielding a Pareto set of solutions that revealed their trade-offs. Hu *et al.* [41] later followed a similar strategy to design structures including cracks at specific locations, where they used bi-directional evolutionary structural optimization (BESO) to update the structural topology and the extended/generalized finite element method (X/GFEM) for the structural analysis. As an alternative to avoid fracture failure by optimizing the topology of the structure with cracks, Klarbring *et al.* [3] optimized an adhesively bonded patch fixed to a structure, thereby minimizing the crack energy release rate. In addition to gradient-based optimization, improving fracture resilience in materials and structures has also been investigated with gradient-free algorithms [42].

Evolving cracks have also been studied in topology optimization, primarily by means of phase-field methods [43–45]. Xia *et al.* [46] maximized fracture resistance of quasi-brittle composites for multiple predefined cracks that were allowed to propagate using a phase-field approach. Russ and Waisman [47] used a phase-field approach within a SIMP-based topology optimization, and minimized the weight of a structure while putting a constraint on the fracture surface energy. The same authors later added the fracture surface energy to the objective function and weighted its priority with a scaling factor [48]. Da and Yvonnet [49] combined BESO with the phase-field method to design a composite material with improved fracture resistance by considering interfacial failure. Instead of using density-based methods, Wu *et al.* [50] incorporated a phase-field fracture model into the level set-based topology optimization to improve a structure's capability to withstand fracture; both crack initiation and propagation were considered during the optimization, which sought to optimize the reinforcement layout in two-phase composite materials. Afterwards, the same authors developed their methodology to include nonlinear finite element analysis (FEA) when designing structures with enhanced fracture resistance [51]. The use of phase-field methods, however, is not without issues [45]. For instance, the length scale parameter used to define the transition zone tends to become small, requiring a very fine mesh especially at the vicinity of a crack. Accurate phase-field models are therefore computationally demanding.

For designing a structure that minimizes the likelihood of fracture, it would be desired to consider the possibility of cracks nucleating anywhere in the computational design domain. However, the design of structures with enhanced fracture resistance, which considers cracks nucleating at many locations under LEFM assumptions, has only been scarcely explored to date. This is mainly because of the vast computational demands required for such a design approach: A single TO iteration would have to evaluate every potential crack nucleating at multiple locations in the solid domain, for instance, by means of FEA with special finite element (FE) meshes tailored to resolve accurately the cracks' singular stress fields. To complicate things further, every potential crack could have an arbitrary orientation. Then ERRs would have to be computed for every potential crack, for example, by means of the J-integral. As a result, such an approach to design is simply intractable. To cope with this limitation, some studies have relied heavily on simplifying assumptions. In shape optimization, Jones *et al.* [52] proposed a modified biological algorithm to obtain the optimal shape of a hole under the assumption that cracks could nucleate only at right angles from it; stress intensity factors (SIFs) were evaluated by the finite element alternating technique, whereby a single FEA of the uncracked body is used together with analytical functions for any crack in a post-processing step [53]. Later, Das *et al.* [54] presented a modified evolutionary structural optimization (ESO) algorithm to optimize the shape of structures for maximum fracture resistance, also allowing cracks nucleating along the boundary but with SIFs calculated using an analytical expression derived by Kujawski [55]. Regarding topology optimization, Challis *et al.* [56] used a failure model that considered *pseudo-cracks* initiating at element nodes along the domain boundary. The objective function for fracture resistance is derived from the change of structural compliance at these locations using the *"virtual crack extension"* technique, whereby element nodes are moved in the direction of the inward normal to the boundary to mimic crack nucleation. They acknowledge that such objective function is close to only considering the energy density of each node in tension along the boundary, which results in similar optimized designs as those obtained from compliance minimization in most cases. To date, no work has attempted to conduct topology optimization under LEFM assumptions, where cracks are allowed to nucleate at many locations in the computational domain.

In this work we propose an LEFM-based topology optimization procedure to design structures with tailored fracture resistance by optimizing an aggregation of ERRs. The methodology builds on our previous work in the context of compliance minimization [57], where we use a level set function to describe topology and the Interface-enriched Generalized Finite Element Method (IGFEM) to analyze the structural response [58]. Cracks are allowed to nucleate perpendicularly to solid-void interfaces, at the location of enriched nodes that are added in IGFEM to resolve the displacement field accurately. ERRs of all potential cracks are obtained by means of topological derivatives [59], for which a *single* FEA of the *uncracked* domain is required. Consequently, topological derivatives are the key ingredient to make the topology optimization tractable. Since an accurate stress field is required to obtain ERRs, we use a stress recovery technique for low-order finite elements to smoothen the stress field [60–62]—and thus avoid the stress overestimation that usually arises in enriched FEM [63]. In this optimization framework, ERRs calculated at each potential crack are aggregated into a single term using the P-mean function [20]. In addition, an alternative formulation based on von Mises stresses is proposed to design structures with uniform stress distribution. Their corresponding analytical sensitivity formulations are derived by using an adjoint formulation. The method of moving asymptotes (MMA) is set as the optimizer to update the design variables [64]. The capability of the proposed technique is showcased on various examples that tailor fracture resistance. First, we solve the shape optimization problem of a square design domain with a hole in the center under biaxial tension; we show the optimal design of a circular hole with a uniform distribution of energy release rates is obtained. Then, the topology of the L-shaped bracket is optimized, where the sharp re-entrant corner in the initial design is removed and a smooth round corner emerges in the optimized design. We compare this result with that of a von Mises stress minimization problem aimed at obtaining a uniform stress distribution. The latter's optimized result also eliminates the sharp re-entrant corner with the stress concentration. Finally, we obtain an optimized design for maximum fracture resistance anisotropy by solving a multiple loading optimization problem; the objective of this problem is to maximize energy release rates when the domain is compressed horizontally, while simultaneously minimize them when compressed vertically.

2. Formulation

Consider an open domain $\Omega \subset \mathbb{R}^2$ (with closure $\overline{\Omega}$), composed of isotropic linear elastic solid material with Young's modulus E_1 and Poisson's ratio ν_1. The domain Ω lies within a fixed domain $\Delta \supset \Omega$, and we denote by $\Delta \setminus \Omega$ as the part of the domain occupied by void with Young's modulus $E_2 \ll E_1$ and Poisson's ratio ν_2. The domain's smooth boundary $\partial\Omega = \Gamma = \overline{\Omega} \setminus \Omega$ consists of two non-overlapping regions Γ_D and Γ_N, where Dirichlet boundary conditions $\bar{\boldsymbol{u}}$ and surface tractions $\bar{\boldsymbol{t}}$ are prescribed, respectively.

The displacement field $\boldsymbol{u}$ is a unique solution to the boundary value problem that describes the static equilibrium, *i.e.*,

$$\begin{cases} \nabla \cdot \boldsymbol{\sigma} + \boldsymbol{b} = \boldsymbol{0} & \text{in } \Omega, \\ \boldsymbol{u} = \bar{\boldsymbol{u}} & \text{on } \Gamma_D, \\ \boldsymbol{\sigma} \cdot \boldsymbol{n} = \bar{\boldsymbol{t}} & \text{on } \Gamma_N, \end{cases} \tag{1}$$

where $\nabla\cdot$ denotes the divergence operator, $\boldsymbol{\sigma}$ Cauchy's stress tensor, $\boldsymbol{b}$ the body force, and $\boldsymbol{n}$ the outward normal to the boundary Γ. Under the assumption of linear elastic material behavior, the stress tensor $\boldsymbol{\sigma}$ is related to strain $\boldsymbol{\epsilon}$ by Hooke's law as $\boldsymbol{\sigma} = \mathbf{C} : \boldsymbol{\epsilon}(\boldsymbol{u})$, where $\mathbf{C}$ is the constitutive tensor, and $\boldsymbol{\epsilon} = \frac{1}{2}(\nabla\boldsymbol{u} + \nabla\boldsymbol{u}^\intercal)$ is the infinitesimal strain tensor.

The weak formulation of this linear elasticity problem is: Find $\boldsymbol{u} \in \boldsymbol{\mathcal{U}}$ such that

$$a(\boldsymbol{u}, \boldsymbol{v}) = \ell(\boldsymbol{v}) \quad \forall \boldsymbol{v} \in \boldsymbol{\mathcal{V}}, \tag{2}$$

where $\boldsymbol{\mathcal{U}}$ is the vector-valued set of kinematically admissible displacement fields and $\boldsymbol{\mathcal{V}}$ the vector-valued space of weight functions that satisfy homogeneous essential boundary conditions on Γ_D. The bilinear $a(\boldsymbol{u}, \boldsymbol{v})$ and linear $\ell(\boldsymbol{v})$ forms, which also represent the virtual work of internal and external forces, respectively, are given by

$$a(\boldsymbol{u}, \boldsymbol{v}) = \int_\Omega \boldsymbol{\epsilon}(\boldsymbol{v}) : \mathbf{C} : \boldsymbol{\epsilon}(\boldsymbol{u}) \, \mathrm{d}\Omega, \tag{3}$$

and

$$\ell(\boldsymbol{v}) = \int_\Omega \boldsymbol{v} \cdot \boldsymbol{b} \, \mathrm{d}\Omega + \int_{\Gamma_N} \boldsymbol{v} \cdot \bar{\boldsymbol{t}} \, \mathrm{d}\Gamma. \tag{4}$$

In order to solve the problem above, the design domain Δ is discretized by finite element such that $\Delta^h = \mathrm{int}(\cup_i e_i)$, where e_i is the ith finite element and $\mathrm{int}(\cdot)$ represents set interior. The finite-dimensional form of Eq. (2) is then

$$\sum_i \int_{e_i} \boldsymbol{\epsilon}(\boldsymbol{v}^h) : \mathbf{C} : \boldsymbol{\epsilon}(\boldsymbol{u}^h) \, \mathrm{d}\Omega = \sum_i \int_{e_i} \boldsymbol{v}^h \cdot \boldsymbol{b} \, \mathrm{d}\Omega + \sum_i \int_{\partial e_i \cap \Gamma_N} \boldsymbol{v}^h \cdot \bar{\boldsymbol{t}} \, \mathrm{d}\Gamma, \qquad \forall \boldsymbol{v}^h \in \boldsymbol{\mathcal{V}}^h \tag{5}$$

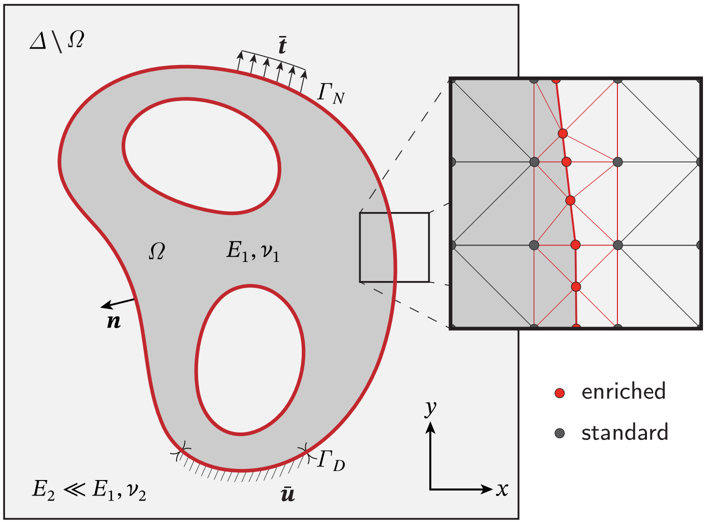

Fig. 1. A solid domain $\varOmega$ with a smooth boundary $\partial\varOmega = \varGamma_D \cup \varGamma_N$ defined in a fixed background domain $\varDelta$. Dirichlet boundary conditions are prescribed on $\varGamma_D$, and surface tractions are prescribed on $\varGamma_N$. For the discretized model, enriched nodes (marked with red circles) are created at intersections between $\partial\varOmega$ and the edges of mesh elements. The integration elements are created near the boundary (marked with red triangles).

where $\boldsymbol{u}^h \in \boldsymbol{\mathcal{U}}^h$ and $\boldsymbol{v}^h \in \boldsymbol{\mathcal{V}}^h$ are the trial solution and weight function, respectively.

In the Interface-enriched Generalized Finite Element Method (IGFEM), the interaction between $\varDelta^h$ and $\varGamma$ creates new (enriched) nodes (marked by red circles in Fig. 1) at intersections between element edges and the boundary. Afterwards, cut elements in $\varDelta^h$ are split into integration elements, which as the name suggests, are used for the numerical quadrature of local stiffness and force arrays. In IGFEM the discrete displacement field $\boldsymbol{u}^h$ is written as

$$\boldsymbol{u}^h = \underbrace{\sum_{i \in \iota_h} N_i(\boldsymbol{x}) \boldsymbol{U}_i}_{\text{standard FEM}} + \underbrace{\sum_{i \in \iota_w} \psi_i(\boldsymbol{x}) \boldsymbol{\alpha}_i}_{\text{enrichment}} . \tag{6}$$

In this equation, the first term is the standard FEM approximation, where ι_h denotes the index set of all nodes in $\varDelta^h$ from the original background mesh (marked by black circles in Fig. 1), and N_i and $\boldsymbol{U}_i$ are the Lagrange shape function and degrees of freedom (DOFs) of the ith mesh node. In the second enrichment term, ι_w represents the index set of enriched nodes, and ψ_i is the enrichment function associated with corresponding enriched DOFs $\boldsymbol{\alpha}_i$.

Regarding the evaluation of the local stiffness matrix $\boldsymbol{k}_e$ and force vector $\boldsymbol{f}_e$, elements that are not intersected follow standard FEM procedures. For integration elements, following a standard isoparametric procedure, $\boldsymbol{k}_e$ and $\boldsymbol{f}_e$ can be evaluated as

$$\boldsymbol{k}_e = \int_e \boldsymbol{B}^\intercal \mathbf{C} \boldsymbol{B} \, j_e \, \mathrm{d}\boldsymbol{\xi}, \quad \text{and} \quad \boldsymbol{f}_e = \int_e \begin{bmatrix} \boldsymbol{N} \\ \boldsymbol{\psi} \end{bmatrix} \boldsymbol{b} \, j_e \mathrm{d}\boldsymbol{\xi} + \int_{\partial e \cap \varGamma_N} \begin{bmatrix} \boldsymbol{N} \\ \boldsymbol{\psi} \end{bmatrix} \bar{\boldsymbol{t}} \, j_e \, \mathrm{d}\partial\boldsymbol{\xi}, \tag{7}$$

where $\boldsymbol{\xi} = (\xi_1, \xi_2)$ is the master coordinate, $\boldsymbol{N}$ and $\boldsymbol{\psi}$ are vectors that stack the element's standard shape functions and enrichment functions, respectively, j_e is the Jacobian determinant (for the integration element's transformation), and $\boldsymbol{B} = \left[\boldsymbol{\varDelta}_{\xi}^\intercal \boldsymbol{N}^\intercal \boldsymbol{J}^{-\intercal} \quad \boldsymbol{\varDelta}_{\xi}^\intercal \boldsymbol{\psi}^\intercal \boldsymbol{J}_e^{-\intercal} \right]$ is the strain–displacement matrix, where $\boldsymbol{J}_e^{-1}$ and $\boldsymbol{J}^{-1}$ are the inverse of the Jacobian of the isoparametric mapping for the integration and parent elements, respectively, and the differential operator $\boldsymbol{\varDelta}_{\xi}$ is given by

$$\boldsymbol{\varDelta}_{\xi} \equiv \begin{bmatrix} \frac{\partial}{\partial \xi_1} & 0 & \frac{\partial}{\partial \xi_2} \\ 0 & \frac{\partial}{\partial \xi_2} & \frac{\partial}{\partial \xi_1} \end{bmatrix}^\intercal . \tag{8}$$

Considering the contribution of all elements in the discretization, the global stiffness matrix $\boldsymbol{K}$ and force vector $\boldsymbol{F}$ are given by

$$\boldsymbol{K} = \underset{i}{\mathbb{A}}\, \boldsymbol{k}_i, \qquad \boldsymbol{F} = \underset{i}{\mathbb{A}}\, \boldsymbol{f}_i, \tag{9}$$

where $\mathbb{A}$ is the standard finite element assembly operator. For more details on IGFEM's formulation see Refs. [58,65].

Similarly to X/GFEM, the complexity of creating a fitted discretization in standard FEM is transferred in IGFEM to the enriched formulation, which requires advanced computational geometry operations for intersecting a usually structured background finite element mesh with the discontinuities. However, although IGFEM retains the main feature of X/GFEM, it also keeps the attractive properties of standard FEM: Since enrichment functions are constructed with Lagrange shape functions of integration elements, their value is exactly zero at original mesh nodes (this property requires shifting in X/GFEM [66,67]). This means that DOFs associated with background mesh nodes represent the displacement at their corresponding location, thus keeping their physical interpretation. Moreover, essential boundary conditions on discontinuities can be prescribed strongly after solving a local problem or via multiple point constraints (MPCs) [68]. For instance, as shown in Fig. 2(a), an original element e with nodes $\boldsymbol{x}_1, \boldsymbol{x}_2$ and $\boldsymbol{x}_3$ is cut by a material interface (shown in red), after which enriched nodes $\boldsymbol{x}_4$ and $\boldsymbol{x}_5$ are created. In order to prescribe the displacement field $\bar{\boldsymbol{u}}$ on nodes $\boldsymbol{x}_1, \boldsymbol{x}_2$ and $\boldsymbol{x}_4$, which are part of Γ_D, we solve for a local problem for the enriched DOFs:

$$\boldsymbol{\alpha}_4 = \bar{\boldsymbol{u}}(\boldsymbol{x}_4) - N_1(\boldsymbol{x}_4)\boldsymbol{U}_1 - N_2(\boldsymbol{x}_4)\boldsymbol{U}_2. \tag{10}$$

Once known, the enriched DOFs are prescribed strongly in the same way as $\boldsymbol{U}_1 = \bar{\boldsymbol{u}}(\boldsymbol{x}_1)$ and $\boldsymbol{U}_2 = \bar{\boldsymbol{u}}(\boldsymbol{x}_2)$. Fig. 2(b) shows another scenario where Γ_D actually crosses the element, which requires prescribing the displacement $\bar{\boldsymbol{u}}$ on enriched nodes $\boldsymbol{x}_4$ and $\boldsymbol{x}_5$ using MPCs. According to Eq. (6), the enriched DOFs are given by

$$\begin{aligned} \boldsymbol{\alpha}_4 &= \bar{\boldsymbol{u}}(\boldsymbol{x}_4) - N_1(\boldsymbol{x}_4)\boldsymbol{U}_1 - N_2(\boldsymbol{x}_4)\boldsymbol{U}_2, \\ \boldsymbol{\alpha}_5 &= \bar{\boldsymbol{u}}(\boldsymbol{x}_5) - N_2(\boldsymbol{x}_5)\boldsymbol{U}_2 - N_3(\boldsymbol{x}_5)\boldsymbol{U}_3. \end{aligned} \tag{11}$$

These two equations can be included in the following system

$$\underbrace{\begin{bmatrix} \boldsymbol{U}_1 \\ \boldsymbol{U}_2 \\ \boldsymbol{U}_3 \\ \boldsymbol{\alpha}_4 \\ \boldsymbol{\alpha}_5 \end{bmatrix}}_{\boldsymbol{U}} = \underbrace{\begin{bmatrix} \boldsymbol{I} & \boldsymbol{0} & \boldsymbol{0} & \boldsymbol{0} & \boldsymbol{0} \\ \boldsymbol{0} & \boldsymbol{I} & \boldsymbol{0} & \boldsymbol{0} & \boldsymbol{0} \\ \boldsymbol{0} & \boldsymbol{0} & \boldsymbol{I} & \boldsymbol{0} & \boldsymbol{0} \\ -N_1(\boldsymbol{x}_4)\cdot\boldsymbol{I} & -N_2(\boldsymbol{x}_4)\cdot\boldsymbol{I} & \boldsymbol{0} & \boldsymbol{0} & \boldsymbol{0} \\ \boldsymbol{0} & -N_2(\boldsymbol{x}_5)\cdot\boldsymbol{I} & -N_3(\boldsymbol{x}_5)\cdot\boldsymbol{I} & \boldsymbol{0} & \boldsymbol{0} \end{bmatrix}}_{\boldsymbol{T}} \underbrace{\begin{bmatrix} \tilde{\boldsymbol{U}}_1 \\ \tilde{\boldsymbol{U}}_2 \\ \tilde{\boldsymbol{U}}_3 \\ \tilde{\boldsymbol{\alpha}}_4 \\ \tilde{\boldsymbol{\alpha}}_5 \end{bmatrix}}_{\tilde{\boldsymbol{U}}} + \underbrace{\begin{bmatrix} \vec{\boldsymbol{0}} \\ \vec{\boldsymbol{0}} \\ \vec{\boldsymbol{0}} \\ \bar{\boldsymbol{u}}(\boldsymbol{x}_4) \\ \bar{\boldsymbol{u}}(\boldsymbol{x}_5) \end{bmatrix}}_{\boldsymbol{g}}, \tag{12}$$

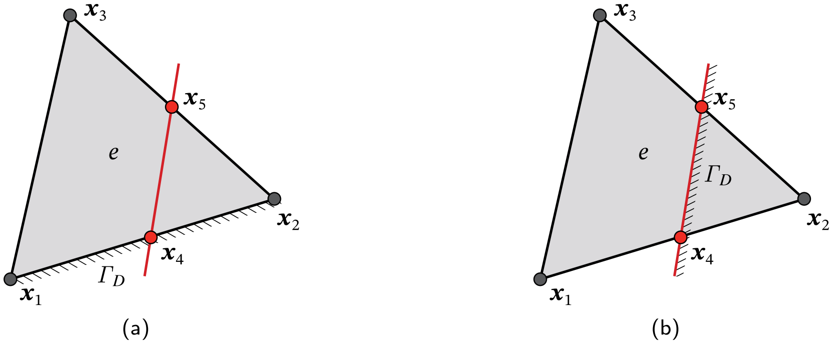

Fig. 2. Boundary region Γ_D with prescribed Dirichlet BCs: (a) Γ_D is aligned with an element edge; and (b) Γ_D cuts through the element. In both cases, two enriched nodes $\boldsymbol{x}_4$ and $\boldsymbol{x}_5$ are created at the intersection between the interface (marked in red) and edges of the background element.

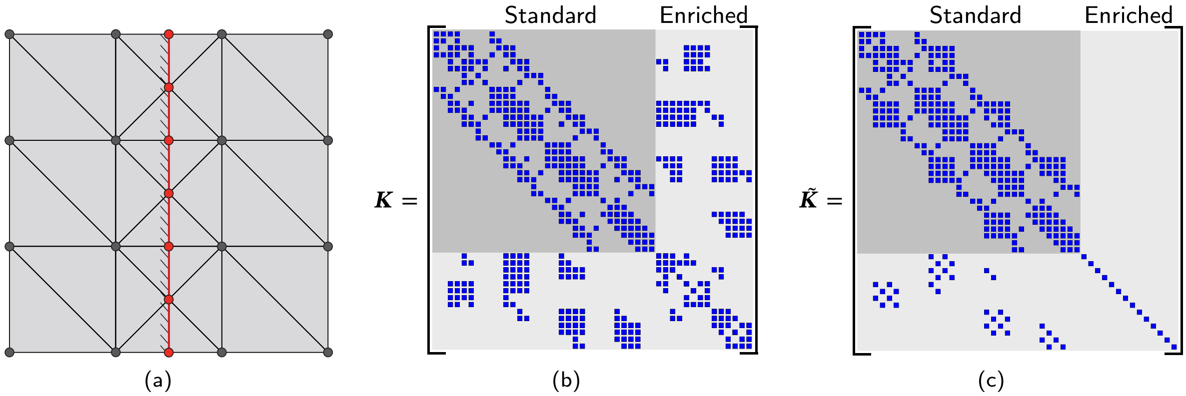

Fig. 3. (a) A background mesh with 3 × 3 × 2 triangular elements intersects an interface (marked in red), where essential boundary conditions are prescribed; (b,c) Non-zeros terms (marked with blue squares) of the global stiffness matrix before (b) and after (c) applying multiple-point constrains.

where $\boldsymbol{I}$ is a 2×2 identity matrix, $\mathbf{0}$ is a zero matrix with the same dimension, and $\vec{\mathbf{0}}$ is a vector with two zero components. $\boldsymbol{T}$ is a transformation matrix containing the relation between original DOFs $\boldsymbol{U}$ and new DOFs $\tilde{\boldsymbol{U}}$, and $\boldsymbol{g}$ is a vector of the prescribed values $\bar{\boldsymbol{u}}$. In this case, the original equilibrium equation $\boldsymbol{K}\boldsymbol{U} = \boldsymbol{F}$, where $\boldsymbol{K}$ and $\boldsymbol{F}$ are the global stiffness matrix and force vector, respectively, is modified to $\tilde{\boldsymbol{K}}\tilde{\boldsymbol{U}} = \tilde{\boldsymbol{F}}$. $\tilde{\boldsymbol{K}}$ and $\tilde{\boldsymbol{F}}$ are expressed as

$$\tilde{\boldsymbol{K}} = \boldsymbol{T}^{\intercal}\boldsymbol{K}\boldsymbol{T}, \quad \text{and} \quad \tilde{\boldsymbol{F}} = \boldsymbol{T}^{\intercal}(\boldsymbol{F} - \boldsymbol{K}\boldsymbol{g}), \tag{13}$$

respectively. If displacement boundary conditions are only prescribed on original mesh nodes, then $\boldsymbol{T}$ is an identity matrix and $\boldsymbol{g}$ is a zero vector, which leads to $\tilde{\boldsymbol{K}} = \boldsymbol{K}$ and $\tilde{\boldsymbol{F}} = \boldsymbol{F}$. The transformation to the stiffness matrix given by Eq. (13) will change the sparsity of the global stiffness matrix. Consider in Fig. 3(a) a background mesh with 3 × 3 × 2 linear triangular elements that is intersected by an interface (marked in red), where Dirichlet boundary conditions are prescribed. The change in sparsity before and after applying MPCs is shown in Fig. 3, where non-zero terms (marked with blue squares) show that no new terms are generated after the transformation.

3. Topology optimization formulation

By means of topology optimization, we seek to solve the following problem:

$$\begin{aligned} &\text{minimize} && J(\boldsymbol{s}) \\ &\text{subject to} && \tilde{\boldsymbol{K}}\tilde{\boldsymbol{U}} = \tilde{\boldsymbol{F}}, \\ & && V_{\mathrm{s}} \leq V_{\mathrm{c}}. \end{aligned} \tag{14}$$

where $J(\boldsymbol{s})$ is an objective function that depends on design variable vector $\boldsymbol{s}$, V_{s} is the volume occupied by solid material, and V_{c} is its maximum allowed value.

The objective function, denoted J henceforth for simplicity, is an aggregation function in P-mean form that collects energy release rates of all potential cracks:

$$J = \left(\frac{1}{N_{\text{node}}} \sum_{i=1}^{N_{\text{node}}} G_i^p \right)^{\frac{1}{p}}, \tag{15}$$

where p is an integer exponent and N_{node} is the number of nodes along external and internal boundaries that are under tension, and G_i is the energy release rate at the ith enriched node.

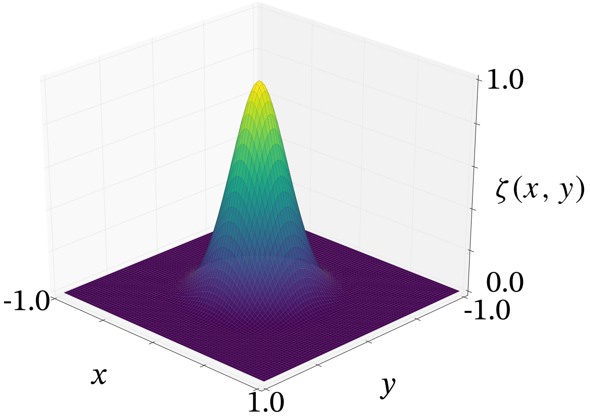

Fig. 4. Radial basis function $\zeta(x, y)$ with center at $(0, 0)$ and support radius $r_s = 0.5$.

3.1. Topology description

In this work the location of the boundary Γ is represented by a level set function ϕ, which was first introduced to structural topology optimization by Sethian and Wiegmann [69]. This implicit function is defined as

$$\begin{aligned} &\phi(\boldsymbol{x}) = 0 \quad \forall \boldsymbol{x} \in \Gamma, \\ &\phi(\boldsymbol{x}) < 0 \quad \forall \boldsymbol{x} \in \Omega, \\ &\phi(\boldsymbol{x}) > 0 \quad \forall \boldsymbol{x} \in \Delta \backslash \overline{\Omega}. \end{aligned} \tag{16}$$

Compactly supported radial basis functions (RBFs) are used to interpolate the level set function for a number of reasons [70]: (i) The smoothness of RBFs results in a smooth level set function; (ii) By increasing the support area of RBFs, each design variable (weight associated with the RBF) has a higher influence on the level set function and thus in the evolution of the material boundary, which can make the optimization process converge faster; (iii) As the RBF grid is decoupled from the finite element discretization of the domain, the design space dimensionality and the background mesh size can be set independently. The level set function $\phi(\boldsymbol{x})$ is then expressed as

$$\phi(\boldsymbol{x}) = \sum_{i=1}^{N_k} \zeta_i(\boldsymbol{x}) s_i, \tag{17}$$

where N_k is the number of RBFs, s_i is the expansion coefficient corresponding to compactly supported RBF $\zeta_i(\boldsymbol{x})$, which has the form [71]

$$\zeta_i(\boldsymbol{x}) = \max\left(0, 1 - r_i\left(\boldsymbol{x}\right)\right)^4 \left(4 r_i\left(\boldsymbol{x}\right) + 1\right), \tag{18}$$

where the scaling parameter $r_i(\boldsymbol{x})$ is defined as $r_i(\boldsymbol{x}) = \|\boldsymbol{x} - \boldsymbol{x}_i\| / r_s$ and r_s is the radius of support.

RBFs are therefore C^2-continuous functions, as shown in Fig. 4: In matrix form, $\phi(\boldsymbol{x}) = \boldsymbol{Z}(\boldsymbol{x})^{\intercal}\boldsymbol{s}$, where $\boldsymbol{Z}(\mathbf{x}) = \begin{bmatrix}\zeta_1(\mathbf{x}) & \zeta_2(\mathbf{x}) & \dots & \zeta_{N_k}(\mathbf{x})\end{bmatrix}^{\intercal}$ and $\boldsymbol{s} = \begin{bmatrix}s_1 & s_2 & \dots & s_{N_k}\end{bmatrix}^{\intercal}$. The design variables for our problem are therefore the coefficients that describe the level set function.

Regarding the update procedure for the level set function, mathematical programming algorithms such as sequential quadratic programming (SQP) [72] and the method of moving asymptotes (MMA) [64], become increasingly popular in level set-based topology optimization [57,73–76]. Because our level set function is parameterized using compactly supported RBFs, it is readily suitable for incorporation in mathematical schemes because of the explicit sensitivities [74]. Therefore, MMA is used to update the design variables, and the optimization terminates when reaching a given maximum number of iterations.

It is worth noting that our procedure is not standard, since the solution of the Hamilton–Jacobi (H–J) equation has traditionally governed the evolution of the topology for level set-based topology optimization procedures [77,78]. However, this first-order partial differential equation is solved by explicit methods with upwind schemes [79,80], where the time step must satisfy the Courant–Friedrichs–Lewy (CFL) condition for stability and convergence [81].

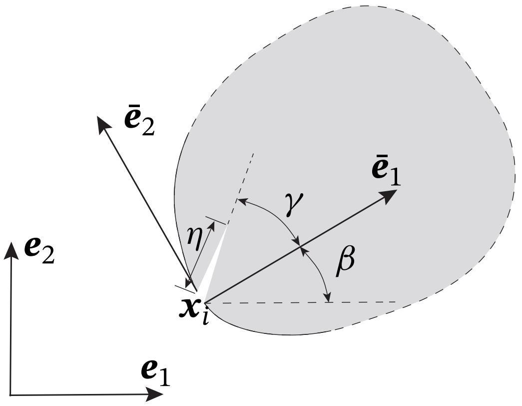

Fig. 5. The illustration of a crack with length η nucleating at node $\boldsymbol{x}_i$, where γ is the angle between this crack and the internal normal of structural boundary, and β is the angle between the global and local coordinate systems.

As a result, updating level set function requires more iterations than our approach, with the consequent increase of computational resources—in addition to the increase in computational time required to solve the H–J equation in each iteration. Moreover, it is necessary to extend the velocity field from the structural boundary to the whole design domain or at least to a narrow band along the boundary [69]. Finally, regularization, which requires solving another H–J equation, should be integrated into the update procedure for obtaining accurate optimized results [82].

3.2. Evaluation of energy release rate

Based on LEFM considerations, the energy release rate G is defined as

$$G = \frac{1}{\overline{E}_1}\left(K_{\mathrm{I}}^2 + K_{\mathrm{II}}^2\right), \tag{19}$$

where $\overline{E}_1 = E_1/\left(1-\nu_1^2\right)$ for plane strain and $\overline{E}_1 = E_1$ for plane stress. K_{I} and K_{II} are the stress intensity factors under modes I and II, respectively. It should be mentioned that negative K_{I} caused by compression stresses is physically incorrect. Then, the corresponding energy release rate is not considered in the objective function. According to Silva *et al.* [59], K_{I} and K_{II} can be computed for an infinitesimal crack at a location $\boldsymbol{x}_i$ along the boundary Γ as

$$\begin{bmatrix} K_{\mathrm{I}}(\boldsymbol{x}_i,\eta,\gamma,\beta) \\ K_{\mathrm{II}}(\boldsymbol{x}_i,\eta,\gamma,\beta) \end{bmatrix} = \sqrt{\pi\eta}\,\underbrace{\begin{bmatrix} h_{11}(\gamma) & h_{12}(\gamma) \\ h_{21}(\gamma) & h_{22}(\gamma) \end{bmatrix}}_{\boldsymbol{H}(\gamma)} \begin{bmatrix} \sigma_{\theta\theta}(\boldsymbol{x}_i,\gamma,\beta) \\ \sigma_{r\theta}(\boldsymbol{x}_i,\gamma,\beta) \end{bmatrix}, \tag{20}$$

where, as illustrated in Fig. 5, η is the crack length, γ is the angle between the crack and the inward normal to the boundary at $\boldsymbol{x}_i$, and β is the angle between the global coordinate system and a local coordinate system located at $\boldsymbol{x}_i$. $h_{ij}(\gamma), i, j \in \{1,2\}$ are sums of trigonometric functions of angle γ [83], and they are given in Appendix A. $\sigma_{\theta\theta}$ and $\sigma_{r\theta}$ are stress components in polar coordinates (r,θ). Eq. (19) can then be rewritten by replacing K_{I} and K_{II} with Eq. (20) as

$$G(\boldsymbol{x}_i,\eta,\gamma,\beta) = \frac{\pi\eta}{\overline{E}_1}\begin{bmatrix} \sigma_{\theta\theta}(\boldsymbol{x}_i,\gamma,\beta) \\ \sigma_{r\theta}(\boldsymbol{x}_i,\gamma,\beta) \end{bmatrix}^{\mathsf{T}} \boldsymbol{H}^{\mathsf{T}}(\gamma)\boldsymbol{H}(\gamma) \begin{bmatrix} \sigma_{\theta\theta}(\boldsymbol{x}_i,\gamma,\beta) \\ \sigma_{r\theta}(\boldsymbol{x}_i,\gamma,\beta) \end{bmatrix}. \tag{21}$$

The energy release rate $G(\boldsymbol{x}_i,\eta,\gamma,\beta)$ as a function of stress $\boldsymbol{\sigma} = \begin{bmatrix}\sigma_{xx} & \sigma_{xy} & \sigma_{xy} & \sigma_{yy}\end{bmatrix}^{\mathsf{T}}$ in global coordinates is

$$G(\boldsymbol{x}_i,\eta,\gamma,\beta) = \frac{\pi\eta}{\overline{E}_1}\boldsymbol{\sigma}(\boldsymbol{x}_i)^{\mathsf{T}}\boldsymbol{Q}(\gamma,\beta)\boldsymbol{\sigma}(\boldsymbol{x}_i), \tag{22}$$

where $\boldsymbol{Q}(\gamma,\beta)$ accounts for the transformation between coordinate systems (see details in Appendix B).

Noteworthy, the results obtained with Eq. (20) are in good agreement with those evaluated via finite element analyses when crack size is smaller than 5% of the domain size [59]. In addition, the accuracy of energy release rates obtained by topological derivatives can be increased by considering high-order terms into the formulation when treating longer cracks [84].

3.3. *Stress calculation*

Because the stress field is obtained by applying the gradient to the displacement field, directly computed stresses from linear finite element solutions are piece-wise constant. Since the stress field plays a critical role in the evaluation of the energy release rate, it is important to use an appropriate method to approximate it. Even though enriched finite element techniques yield more accurate solutions than those obtained by the Ersatz material approach [85], they could also yield poor approximation for the stress field when interfaces get arbitrarily close to background mesh nodes.

To circumvent the issue, several pre- and post-processing techniques have been proposed. One approach is to eliminate small elements by merging nodes in close proximity into a single node [86–88]. This approach can totally prevent the overestimation of the stress, but it requires meddling with the mesh or the interfaces. Another strategy smoothens the stress of an element with small areas by taking its neighboring elements into account. For instance, an average-weighted formulation considering element areas can be used to post-process the stress of these tiny elements [89]. Although this method can provide quite good approximations [90], it does not avoid stress overestimation completely. Yet another technique interpolates the stress field by using stress recovery approaches, such as the superconvergent patch recovery technique [87,91]. Even though sensitivities of the objective function with respect to design variables become intricate, the evaluation of the recovered stress field is more accurate than other techniques.

In this work a new stress recovery technique for low-order finite elements, named the Stress Improvement Procedure (SIP), is adopted to smoothen the stress field [60,61]. SIP is derived from a mixed formulation based on the Hu–Washizu principle [92]. It relaxes the stress-strain relationship point-wise, but enhances the fulfillment of equilibrium. For evaluating the recovered stress in each element, a patch of neighboring elements is detected first. Then the improved stress is obtained by (i) satisfying equilibrium in a weak sense in this patch; and (ii) projecting the directly computed FE stresses into the space of the enhanced stress [61]. Noteworthy, because the enhanced stress space is quadratic, convergence rates are higher than directly computed stresses obtained from linear approximations.

Mathematically, the enhanced stress is computed as $\boldsymbol{\sigma}_e = \boldsymbol{E}_\sigma \hat{\boldsymbol{\sigma}}$, where $\hat{\boldsymbol{\sigma}}$ is a 18×1 vector of stress coefficients computed by solving

$$\left[\sum_{\{e\in\mathcal{E}\}} \begin{pmatrix} \displaystyle\int_e \bar{\boldsymbol{E}}_\sigma^\intercal \boldsymbol{E}_\sigma \,\mathrm{d}e \\ \displaystyle\int_e \boldsymbol{E}_\zeta^\intercal \boldsymbol{\partial}_\sigma \boldsymbol{E}_\sigma \,\mathrm{d}e \end{pmatrix}\right] \hat{\boldsymbol{\sigma}} = \left\{\sum_{\{e\in\mathcal{E}\}} \begin{pmatrix} \displaystyle\int_e \bar{\boldsymbol{E}}_\sigma^\intercal \boldsymbol{\sigma}_e^h \,\mathrm{d}e \\ \displaystyle -\int_e \boldsymbol{E}_\zeta^\intercal \boldsymbol{b} \,\mathrm{d}e \end{pmatrix}\right\}, \tag{23}$$

where $\mathcal{E}$ is the calculation domain (*i.e.*, a patch of elements), $\boldsymbol{E}_\sigma$, $\bar{\boldsymbol{E}}_\sigma$, and $\boldsymbol{E}_\zeta$, are interpolation matrices, $\boldsymbol{\partial}_\sigma$ is a differential operator, and $\boldsymbol{\sigma}_e^h$ is the directly computed stress of the eth element (more details are provided in Appendix C). Considering the interpolation matrices and the differential operator, the maximum polynomial order in the integrands is quartic, which requires six integration points for exact quadrature.

It should be mentioned that only elements with the same material properties are considered when constructing the calculation domain, since different materials are assigned to the solid and void parts. For instance, as shown in Fig. 6(a), a patch of $N_p = 8$ elements (shown in darker shade) is used to recover the stress in the hatched element. In order to evaluate the nodal stress $\boldsymbol{\sigma}(\boldsymbol{x}_i)$ (shown in red in Fig. 6(b)), we find a patch of elements connected to this node first. Then, $\boldsymbol{\sigma}(\boldsymbol{x}_i)$ is calculated based on the recovered stress as

$$\boldsymbol{\sigma}(\boldsymbol{x}_i) = \frac{\sum_{\{e\in\mathcal{E}_i\}} \boldsymbol{\sigma}_e(\boldsymbol{x}_i)}{N_i}, \tag{24}$$

where $\mathcal{E}_i$ is the calculation domain, $\boldsymbol{\sigma}_e(\boldsymbol{x}_i) = \mathbf{E}_\sigma(\boldsymbol{x}_i)\hat{\boldsymbol{\sigma}}_e$ the stress of the eth element evaluated at the ith node, and N_i the number of elements in the node patch.

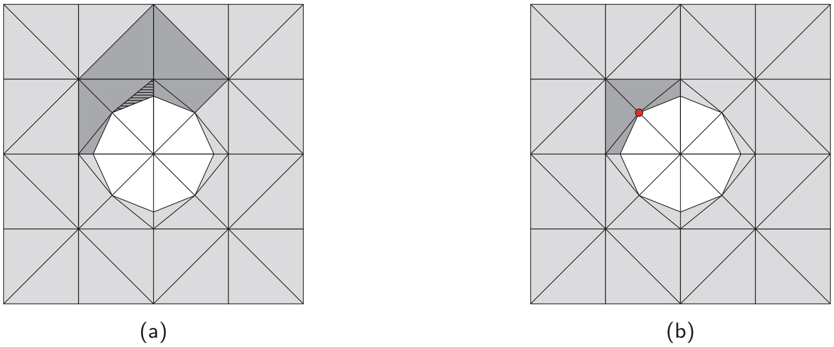

Fig. 6. (a) A patch of elements (marked in darker shade) is used to recover the stress of the target element (hatched); (b) Elements (in darker shade) used to evaluate the stress of a node (marked with a red circle).

3.4. Sensitivity

The sensitivity of the objective function J with respect to design variables $\boldsymbol{s}$ is derived by using the adjoint variable method. A Lagrangian function of the objective, which is constructed by using the adjoint vector $\boldsymbol{\lambda}$, is expressed as $L = J + \boldsymbol{\lambda}^{\mathsf{T}}(\tilde{\boldsymbol{K}}\tilde{\boldsymbol{U}} - \tilde{\boldsymbol{F}})$. Then the derivative of L with respect to the jth design variable s_j is given by

$$\begin{aligned}\frac{\mathrm{d}L}{\mathrm{d}s_j} &= \frac{\partial J}{\partial s_j} + \frac{\partial J}{\partial \tilde{\boldsymbol{U}}}\frac{\partial \tilde{\boldsymbol{U}}}{\partial s_j} + \boldsymbol{\lambda}^{\mathsf{T}}\left(\frac{\partial\left(\tilde{\boldsymbol{K}}\tilde{\boldsymbol{U}}\right)}{\partial s_j} - \frac{\partial \tilde{\boldsymbol{F}}}{\partial s_j}\right) \\ &= \frac{\partial J}{\partial s_j} + \left(\frac{\partial J}{\partial \tilde{\boldsymbol{U}}} + \boldsymbol{\lambda}^{\mathsf{T}}\tilde{\boldsymbol{K}}\right)\frac{\partial \tilde{\boldsymbol{U}}}{\partial \boldsymbol{s}_j} + \boldsymbol{\lambda}^{\mathsf{T}}\left(\frac{\partial \tilde{\boldsymbol{K}}}{\partial s_j}\tilde{\boldsymbol{U}} - \frac{\partial \tilde{\boldsymbol{F}}}{\partial s_j}\right).\end{aligned} \tag{25}$$

In order to obtain the adjoint vector $\boldsymbol{\lambda}$, the following adjoint equation is solved:

$$\frac{\partial J}{\partial \tilde{\boldsymbol{U}}} + \boldsymbol{\lambda}^{\mathsf{T}}\tilde{\boldsymbol{K}} = 0. \tag{26}$$

Details about the evaluation of $\partial J/\partial s_j$, and $\partial J/\partial \tilde{\boldsymbol{U}}$ are given in Appendix D.1. $\partial \tilde{\boldsymbol{K}}/\partial s_j$ and $\partial \tilde{\boldsymbol{F}}/\partial s_j$ are explained in detail in Appendix D.2.

4. Numerical examples

In this section, several numerical examples are investigated to demonstrate the capability of the proposed approach in obtaining designs with tailored fracture resistance. The crack length is set to 1% of the domain size to ensure the validity of Eq. (20). No units are given to material properties, tractions, nor domain dimensions, so results can be interpreted in any consistent unit system. If not explicitly specified, Young's moduli are taken as $E_{\mathrm{s}} = 1$ and $E_{\mathrm{v}} = 10^{-6}$ for solid and void materials, respectively. The Poisson's ratio for both materials is $\nu = 0.3$. Linear triangular elements are used to discretize the design domain—for which a single Gauss point is sufficient in standard and integration elements—and the finite element analysis is conducted under plane strain conditions. Topological gradient information, which has traditionally been used to nucleate holes in the interior of the design domain during topology optimization [93,94], is not considered in the proposed procedure. Therefore, all examples start with an initial design seeded with holes.

4.1. Biaxial tension example

Firstly, a shape optimization example is studied, where unit magnitude tractions $\boldsymbol{t}_1$ and $\boldsymbol{t}_2$ are applied on the sides of a 2 × 2 square domain as illustrated in Fig. 7. Because the design region is immersed into a background domain, the tractions are prescribed by properly integrating the force vector in cut elements, as described in Section 2. Due to symmetry, only a quarter of the design domain is considered with symmetric boundary conditions. A value $p = 8$

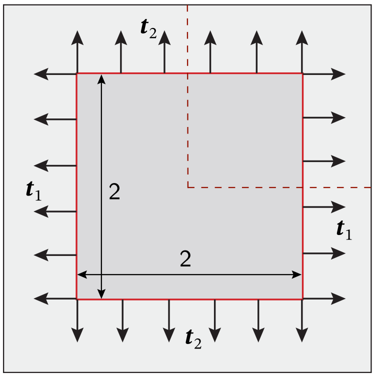

Fig. 7. Schematic of the biaxial tension example with tractions t_1 and t_2 prescribed to edges of a square design domain as shown. The design domain is immersed into a larger background domain that is discretized by constant strain triangles. Due to symmetry, only a quarter of this domain is considered.

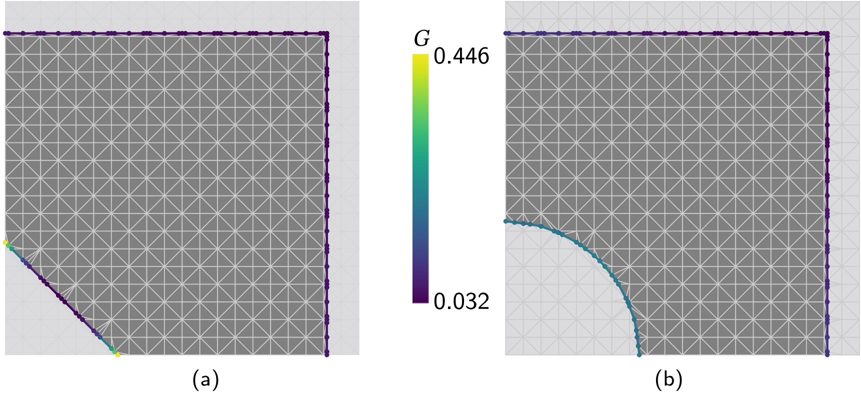

Fig. 8. (a) Initial design with a triangular hole, where energy release rates around top and right vertices of the triangle are much higher than those at other places in the initial design; (b) Optimized design with a quarter of circle, where the distribution of energy release rates is uniform along the material interface in the optimized structure.

is used in the objective function, and the volume of solid material is constrained at $V_c = 0.875$. A background mesh with $20 \times 20 \times 2$ linear triangular elements is used to discretize the background domain, and the maximum number of iterations is set to 100.

Fig. 8(a) shows the initial design, which has a hole with triangular shape at the bottom-left corner. The corresponding optimized design with a quarter of a circular hole is displayed in Fig. 8(b). Figs. 8(a)–8(b) also show their corresponding energy release rate distributions. From Fig. 8(a), it can be seen that energy release rates around top and right vertices of the triangle are much higher than elsewhere because of the stress concentrations. However, energy release rates in the optimized design are uniform along the circular boundary. The convergence for both the objective and material volume fraction is shown in Fig. 9, where it can be seen that the former converges at around 50 iterations. Structures obtained at 10, 30, and 50 iterations are also displayed in the figure. Note that even though the volume of the optimized design is not the same as the constrained value, the constraint is still satisfied; although the MMA optimizer minimizes the objective and satisfies the volume constraint in parallel, it assigns higher priority to the former as a relatively small Lagrange multiplier is associated with the latter. The inset in Fig. 9 shows how the volume increases after 45 iterations.

4.2. L-shaped bracket

We investigate the performance of the proposed method in optimizing the topology of an L-shaped bracket, domain that is also immersed in a square computational domain with dimensions 11×11. The latter is discretized

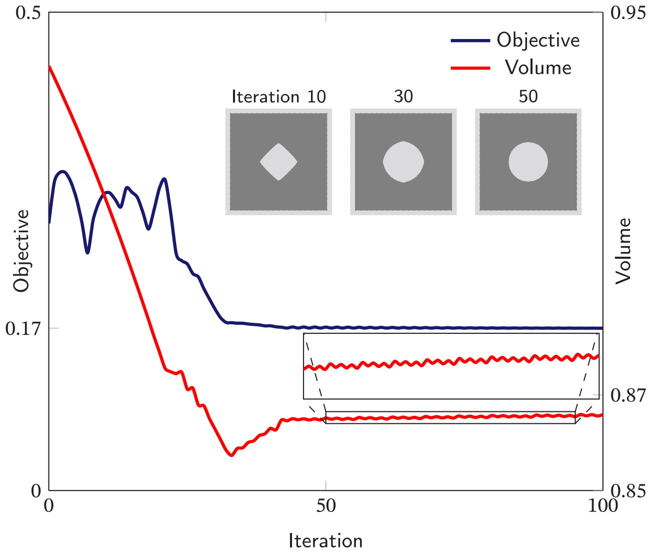

Fig. 9. Convergence for the biaxial tension example shows that the objective function converges at about 50 iterations. Designs obtained after 10, 30, and 50 iterations are displayed.

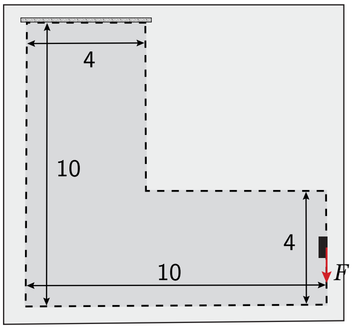

Fig. 10. The schematic of L-shaped bracket example where the top part is fixed and a loading $\|\boldsymbol{F}\| = 0.25$ is applied on the middle of the right side.

with a background FE mesh composed of 100 × 100 × 2 constant strain triangles. As shown in Fig. 10, the area outside the L-shaped bracket, together with a small area in the vicinity of the applied load, is considered as a non-design domain. A homogeneous Dirichlet boundary condition is prescribed along the immersed top edge of the bracket, as discussed in Section 2, and a vertical downward load $\boldsymbol{F} = -1/4\,\boldsymbol{e}_2$ is applied to the middle of right side. A value $p = 8$ is used in the objective function, and the volume constraint is set to $V_c = 25.6$ (40% of the volume of the L-shaped bracket fully occupied by solid material). The maximum number of iterations is set to 500, and the initial design with many circular holes is shown in Fig. 11(a).

The optimized structure is shown in Fig. 11(b), and the corresponding energy release rate distribution is given in the same figure. It can be seen that the sharp internal corner in the initial design with high energy release rate has been removed. At this location, a rounded corner appears in the final result with a uniform distribution of energy release rate values. Fig. 11(b) shows zigzagging of some edges in the optimized design where the level set function is not perfectly smooth. This approximation artifact, which actually improves the objective function, is caused by the discretization. This issue is discussed in detail by van den Boom *et al.* [57]. The convergence curves and optimized structures obtained at 50, 100, 200, and 300 steps are shown in Fig. 12. Oscillations of the objective function are observed during the optimization, particularly at the beginning. Since energy release rates are obtained from the stress field, these oscillations are caused by elements with high stress values. Although the stress recovery technique is used to smoothen the stress field, avoiding stress overestimation caused by bad aspect ratios

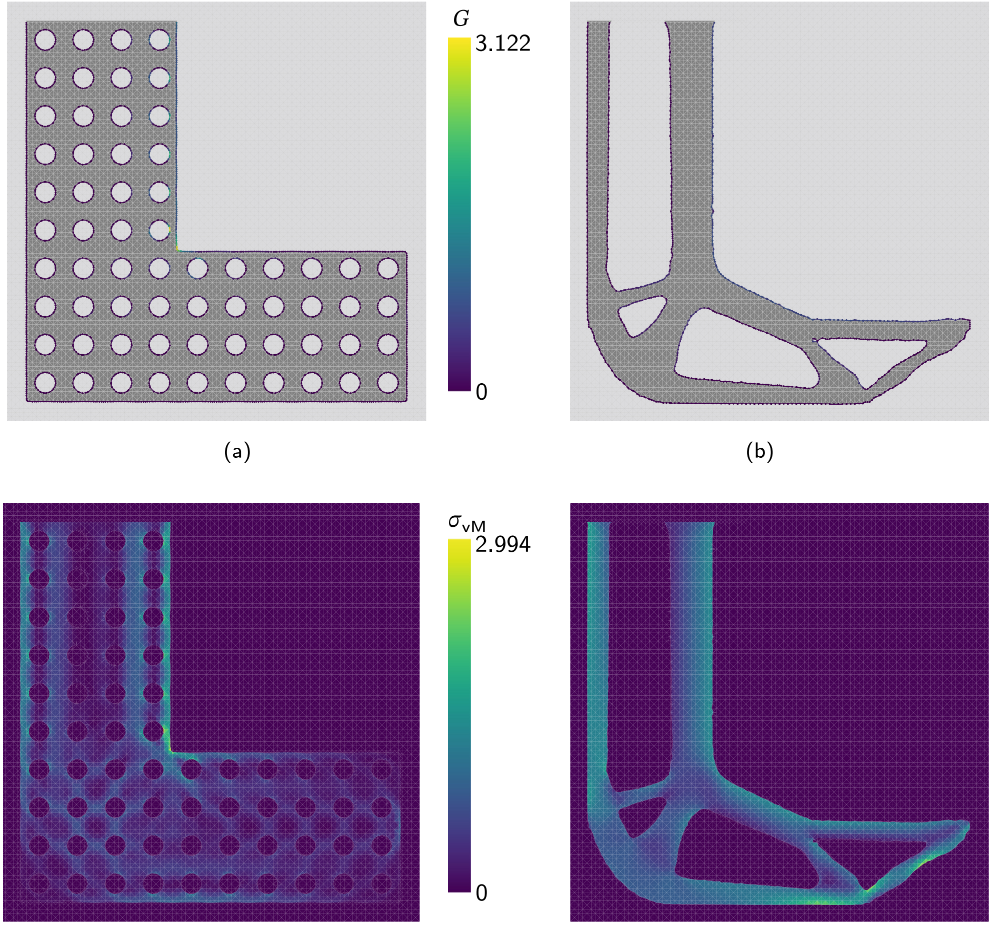

(a) (b)

(c) (d)

Fig. 11. (a) Initial design and its corresponding distribution of energy release rate; (b) Final design obtained with minimizing the energy release rate and its corresponding distribution; The von Mises stress distributions of (c) the initial and (d) optimized designs.

of integration elements, the merging of holes in the initial design is responsible for thin solid structures with high stresses. An optimized design obtained after setting the crack length to 0.5% of the domain size is also shown in Fig. 13(a), where it can be seen that the final result has the same topology with slightly different shapes compared to the original optimized design of Fig. 13(b). The maximum value of the energy release rate of the new design is almost half of that obtained by the original optimized structure—notice the linear relationship between the crack length and the energy release rate in Eqs. (21) and (22). It is worth noting that the optimization is very sensitive to the move limit of the MMA optimizer. If a large move limit is used, the final design could be disconnected, which is actually beneficial to the objective function because stress is nil in isolated regions. A way to eliminate this effect is to consider the structural compliance as a constraint [95]. In addition, we also show the von Mises stress distribution of initial and optimized designs in Figs. 11(c) and 11(d), respectively. It is worth noting that while there are locations with high stresses in the optimized structure, energy release rates are low and therefore the L-shaped bracket will not fracture.

Because energy release rates are derived from the stress field, one may wonder how optimized structures compare with those obtained via stress optimization. Consider the following von Mises stress-based objective function $J_{\sigma_{\text{vM}}}$, which aims at obtaining a uniform stress throughout the entire domain:

$$J_{\sigma_{\text{vM}}} = \frac{1}{N_e} \sum_{i=1}^{N_e} \left(\sigma_{\text{vM}i} - \bar{\sigma}_{\text{vM}}\right)^q , \tag{27}$$

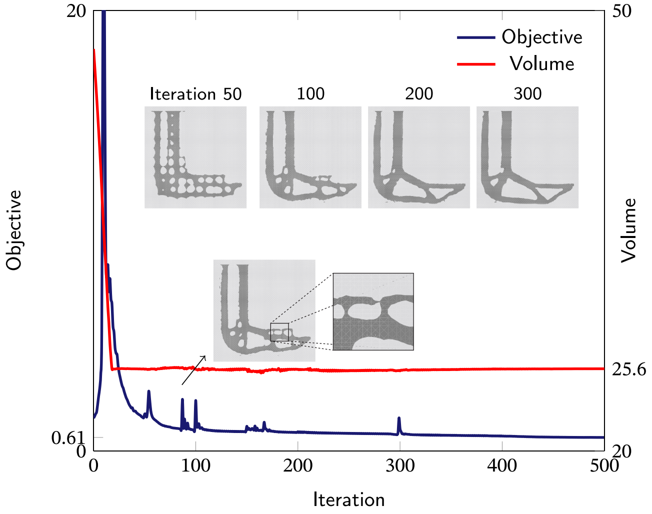

Fig. 12. Convergence plot of objective and volume when optimizing the energy release rate; optimized designs obtained at 50, 100, 200, and 300 iterations; the design obtained after 87 iterations with a thin solid structure.

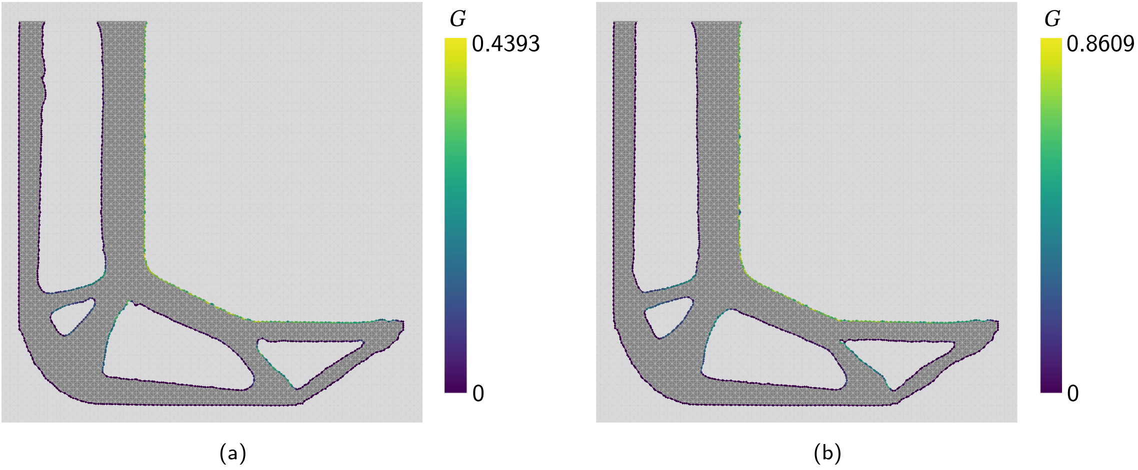

(a)

(b)

Fig. 13. Final designs obtained assuming cracks with lengths of 0.5% (a) and 1% (b) of the domain size. The same structural topology is obtained.

where N_e is the number of elements in the design domain with solid material, and q is an integer exponent, $\sigma_{\mathrm{vM}i}$ is the von Mises stress of the ith element, and $\bar{\sigma}_{\mathrm{vM}}$ is the average von Mises stress of all elements in the solid part. Detailed sensitivity formulations for this objective function with respect to design variable $\boldsymbol{s}$ and displacement field $\tilde{\boldsymbol{U}}$ are given in Appendix D.3. For consistency, we set q to have the same value of p. The same initial design is used as well, with the corresponding von Mises stress field shown in Fig. 11(c). The final design obtained with the above objective function is given in Fig. 14(a), where a round corner also emerges to remove the stress concentration. In addition, Fig. 14(b) shows the energy release rate distribution of the final design with the maximum value 0.8352, which is smaller than the optimized result 0.8609 given in Fig. 11(b). As a lower value of maximum energy release rate is obtained when optimizing the stress distribution, it is apparent that the final design obtained when optimizing the energy release rate is a local optimum. The corresponding von Mises stress distribution, which is relatively smooth near the rounded corner, is shown in the same figure. The convergence plot and structural topologies obtained at 50, 100, 200 and 300 steps are shown in Fig. 15, this time in semi-log scale because there are several orders of magnitude between the objective function values of initial and final designs. Since the value of q is set to 8, this objective is a highly non-linear function of the stress field. Therefore, if the difference between

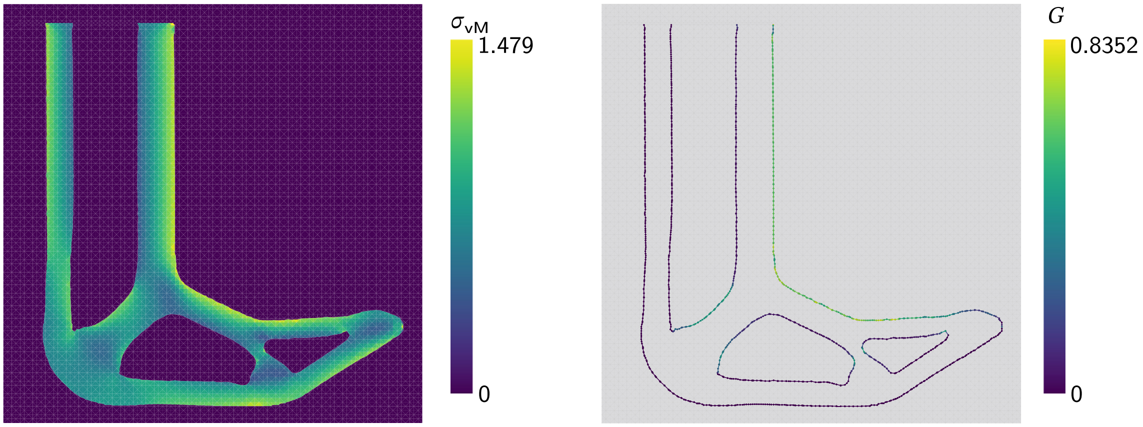

(a) (b)

Fig. 14. Final structure obtained by optimizing the difference between elemental and average von Mises stresses. (a) von Mises stress distribution in the optimized design; (b) energy release rates along the boundary.

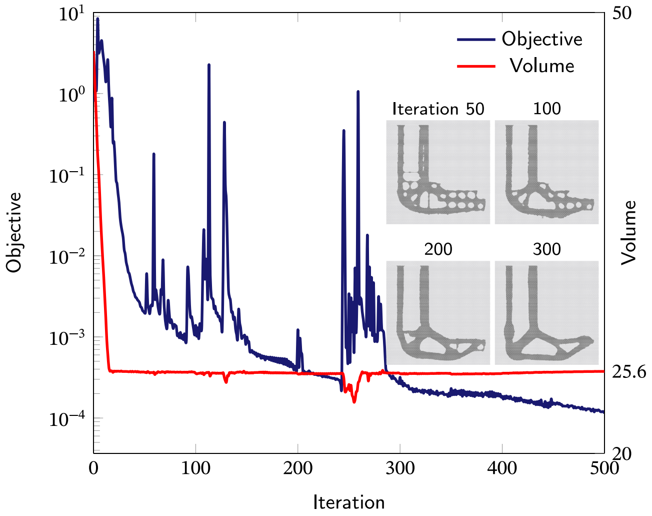

Fig. 15. Convergence plot of objective and volume when optimizing the von Mises stress distribution and optimized designs obtained at 50, 100, 200, and 300 iterations.

elemental and averaged von Mises stresses $\sigma_{\mathrm{vM}i} - \bar{\sigma}_{\mathrm{vM}}$ is greater than 1, the objective could be a large value. Conversely, if the difference is smaller than 1 the objective function approaches zero very rapidly. Moreover, the thin solid structures with stress concentration appear in the optimization process (see Fig. 16(a)), which may result in peak objective values. In addition, the sudden change of the topology in the local region adjusts the loading path (see Figs. 16(b) and 16(c)), which leads to the stress redistribution nearby. We then observe more oscillations during the optimization.

4.3. Fracture resistance anisotropy

The purpose of this example is to obtain an optimized design with fracture resistance anisotropy. In order to achieve this, a multiple-loading optimization problem is set up, where two unit magnitude compressive tractions $\boldsymbol{t}_1$ and $\boldsymbol{t}_2$ are applied in two independent load cases, as shown in Fig. 17. Therefore, two different finite element analyses are performed to obtain the structural solutions $\boldsymbol{u}_1^h(\boldsymbol{x})$ and $\boldsymbol{u}_2^h(\boldsymbol{x})$. Only a quarter of design domain is considered with dimensions 1×1. In order to introduce fracture resistance anisotropy, energy release rates

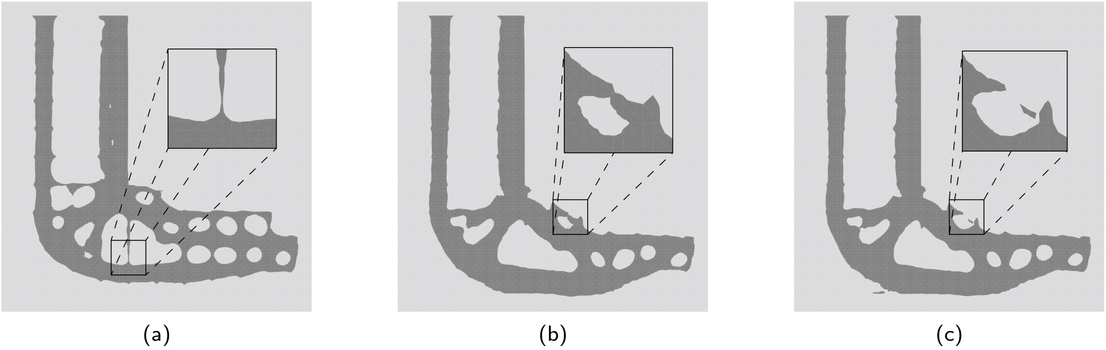

Fig. 16. (a) Thin solid structure with high stress obtained at iteration 59; (b,c) The stress field is redistributed in the local area marked with a black square from (b) 127 to (c) 128 steps, which leads to a high stress distribution nearby.

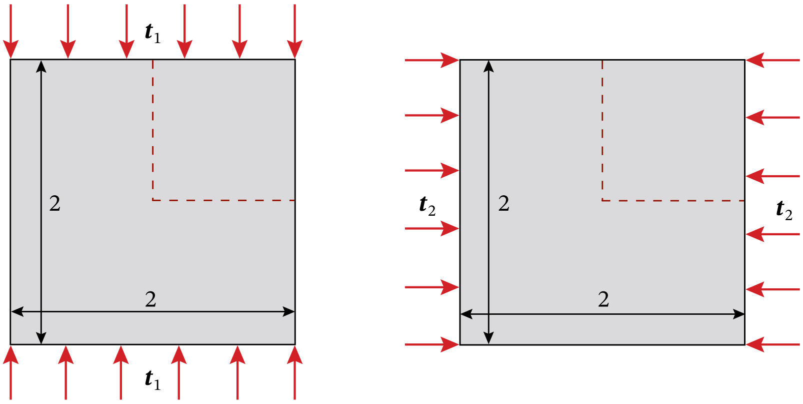

Fig. 17. A domain with dimension 2 × 2 under compression, where $\boldsymbol{t}_1$ and $\boldsymbol{t}_2$ are prescribed on the vertical and horizontal directions, respectively. Under the finite element analysis, a quarter of domain (marked with red dashed segments) is considered.

are minimized when compressing the computational domain along the vertical direction and maximized when compressed along the horizontal direction. This optimization, which is different from previous examples, is formally written as

$$\begin{aligned} \text{minimize} \quad & J = J_1 + J_2 = \frac{1}{N_{\text{node}}} \sum_{i=1}^{N_{\text{node}}} G_{1i} - \frac{1}{N_{\text{node}}} \sum_{i=1}^{N_{\text{node}}} G_{2i} \\ \text{subject to} \quad & \boldsymbol{K}_1 \boldsymbol{U}_1 = \boldsymbol{F}_1, \\ & \boldsymbol{K}_2 \boldsymbol{U}_2 = \boldsymbol{F}_2, \\ & V_{\text{s}} \leq V_{\text{c}}. \end{aligned} \tag{28}$$

In this equation, J_i, $i = \{1, 2\}$ is therefore an aggregation of energy release rate values for the corresponding boundary value problem $\boldsymbol{K}_i \boldsymbol{U}_i = \boldsymbol{F}_i$. Since these quantities are always positive, the negative sign is introduced to the second term J_2 to maximize energy release rates for the horizontal load case. Solid material is constrained at $V_{\text{c}} = 0.5$.

Fig. 18(a) shows the initial design including four holes in the whole domain (only one hole in the actual computational domain) where the ratio $J_2/J_1 = -1$. The corresponding final design in Fig. 18(b) displays that more solid material is placed in along the vertical direction to make the structure tougher. Conversely, there are tiny bars that greatly contribute to maximizing energy release rates for the horizontal load case. For the optimized design, the ratio $J_2/J_1 = -14.85$. The convergence plot about J_1 and J_2 is given in Fig. 19, where J_1 increases and J_2 decreases throughout the optimization. Since the magnitude of J_2 is larger than that of J_1, the optimizer gives priority to the former.

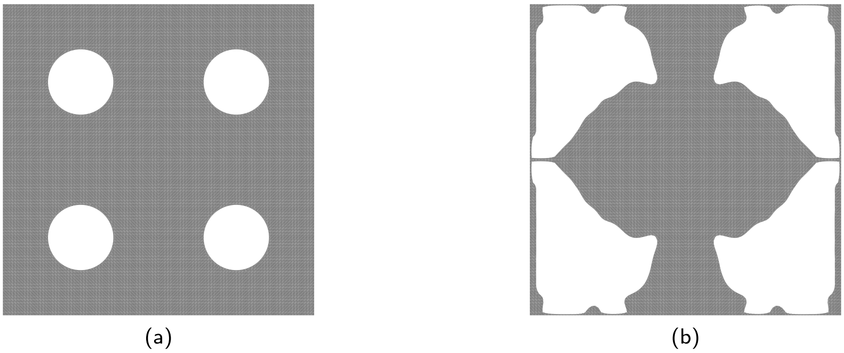
(a) (b)

Fig. 18. (a) Initial design with four holes in the whole domain where the ratio $J_2/J_1 = -1$; (b) The corresponding optimized design with $J_2/J_1 = -14.85$.

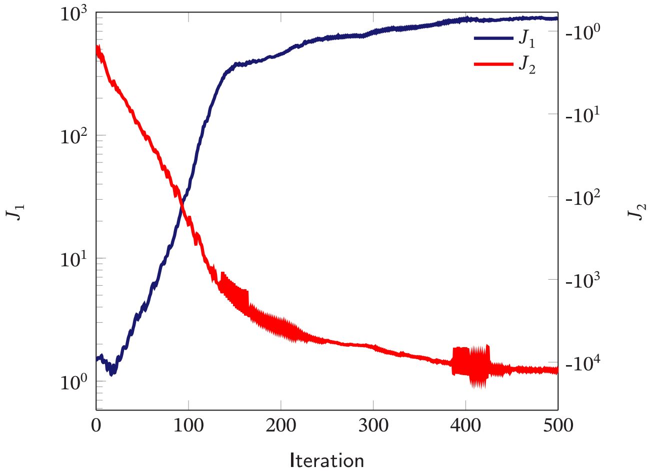

Fig. 19. Convergence plot of J_1 and J_2 when optimizing the fracture resistance anisotropy.

5. Summary and conclusions

In this paper we introduced a novel topology optimization procedure to design structures with tailored fracture resistance. The methodology uses a level set function discretized by radial basis functions to describe the topology, and an enriched finite element formulation to perform structural analysis. Contrary to other works, we do not predefine the location of cracks but instead assume these can nucleate perpendicularly to the structural boundary at discrete locations. Energy release rates of all potential cracks are then evaluated by conducting a single enriched finite element analysis of the intact uncracked model by means of topological derivatives. Since the stress field is used in the latter's formulation, a stress recovery technique was proposed to enhance the stress field and thus overcome the issue of stress overestimation that burdens IGFEM—and other enriched FEMs alike. Since energy release rate is a local quantity, a P-mean aggregation function is used to build the objective function. Because in IGFEM it is straightforward to prescribe essential boundary conditions along discontinuities, the topology optimization can be performed by fully immersing the design domain into a background mesh.

By means of a shape optimization example, we showed that the proposed method recovers the optimal solution of a square plate with a circular hole, along which energy release rate values are uniform. Subsequently, an L-shaped bracket was embedded into a square computational domain discretized via a structured mesh. It was shown how the methodology removed in the final design the sharp inner corner with the stress concentration. Moreover, another objective function associated with von Mises stress was introduced to design a structure with a stress distribution as uniform as possible, which also removed the stress concentration by rounding the corner of the initial design. Finally, a multiple-loading optimization problem was used to design a structure with fracture resistance anisotropy. The technique was able to obtain a design that simultaneously maximized energy release rates when compressing the computational design horizontally while minimizing them when compressing vertically. As a result, the optimized structure is much tougher when compressing the structure vertically.

These are our final remarks:

- The methodology assumes that cracks could only nucleate at right angles from the boundary. However, as discussed by Silva *et al.* [59], there are situations where this is not the most critical angle for crack nucleation. Our work could therefore be extended to find the critical angle for each potential crack, albeit at the expense of more computational resources and a more complex analytical sensitivity formulation.
- We used the P-mean function to aggregate all energy release rates calculated along the structural boundary. However, the value of p affects the optimized result significantly. For instance, for $p = 2$ the sharp re-entrant corner in the L-bracket is not smoothened. Even though the energy release rate around that area has the highest value, the objective function approximates the maximum value inaccurately. While the aggregation function approaches to the maximum value as p is increased, the function also becomes highly nonlinear and could thus lead to instabilities. As a result, there is always a tradeoff between the accuracy of approximating the maximum value and the stability of the methodology.
- We also used an alternative objective function based on von Mises stress. The rationale behind obtaining a structure with a stress distribution as uniform as possible was to make the best use of material. Even though we did not perform the optimization for different values of the exponent q, optimized designs for this problem proved to be quite sensitive to this value, as found elsewhere with a similar stress-based formulation [96].
- The accuracy of energy release rates obtained by means of topological derivatives depends on the accuracy of the stress field. As a result, it is critical to choose an appropriate methodology to avoid stress oscillations during the optimization process that could degenerate the final design. The stress recovery technique adopted in this work cannot only prevent these issues, but also provide more accurate stresses than directly-calculated stresses obtained by applying the gradient to the FE solution. However, the recovery technique also increases the complexity of the sensitivity formulation, which is the most intricate part of this work. For instance, in order to obtain the sensitivity of recovered stresses with respect to design variables, the derivative of Eq. (23) used to evaluate the enhanced stress field should also be calculated, which makes the sensitivity formulation involved.
- Owing to properties of IGFEM, such as creating enriched nodes along discontinuities and using Lagrange shape functions of integration elements to construct enrichments, immersing design domains into any computational FE mesh gives tremendous flexibility. Even though we use the proposed method to obtain solid-void topologies, void material is still assigned to void areas to avoid ill-conditioned stiffness matrices. However, the proposed procedure can be extended to solve pure solid optimization problems by using techniques presented by van den Boom *et al.* [68].
- Compared to a stress-based optimization that considers stress values in all solid elements in the computational domain, our approach to optimize for fracture resistance only considers the evaluation of energy release rates along the boundaries. As a result, as the problems increase in size, asymptotically our approach is more efficient because it computes quantities in lower-dimensional manifolds. In addition, only enriched nodes under tension are considering when evaluating the objective function. To remain competitive, a stress-based optimization procedure would have to consider only the stress in solid elements crossed by interfaces. Nevertheless, such an approach would mandate for a procedure that detects such elements, complicating the computer implementation.
- Designing structures with enhanced fracture resistance in 3D could also be done by developing the proposed topology optimization methodology. To that end, the most intricate part would be to obtain the formulation for the topological derivatives, for which some progress has already been made [97]. In addition, extra efforts are required to obtain the analytical sensitivity formulation for recovered stresses in 3D.

Table 1
Data of parameters $c_i^{(\mathrm{I},1)}$, $c_i^{(\mathrm{II},1)}$, $c_i^{(\mathrm{I},2)}$, and $c_i^{(\mathrm{II},2)}$ in matrix $\boldsymbol{H}(\gamma)$.

i	$c_i^{(\mathrm{I},1)}$	$c_i^{(\mathrm{II},1)}$	$c_i^{(\mathrm{I},2)}$	$c_i^{(\mathrm{II},2)}$
1	−0.174856	−0.198196	−0.419098	0.478653
2	1.393783	0.681479	−0.197271	−0.130868
3	−0.278259	−0.282608	−0.445897	0.663435
4	0.240695	0.136522	−0.050066	−0.066599
5	−0.071883	−0.041562	−0.022856	0.183693
6	0.011246	0.006177	0.003281	−0.006140

Declaration of competing interest

The authors declare the following financial interests/personal relationships which may be considered as potential competing interests: Jian Zhang reports financial support was provided by China Scholarship Council.

Acknowledgment

Jian Zhang would like to thank China Scholarship Council (CSC NO. 201606060130) for the financial support.

Appendix A. Matrix $\boldsymbol{H}(\gamma)$ of influence coefficients

$\boldsymbol{H}(\gamma)$ is a 2 × 2 matrix that is a function of angle γ between cracks and the inward normal of the structural boundary [83]. Its components are

$$
\begin{aligned}
h_{11}(\gamma) &= \sum_{i=1}^{6} \left\{ \left[1-\tan(\gamma)^2\right] \cdot c_i^{(\mathrm{I},1)} \cos[(i-1)\gamma] - \frac{\sin(\gamma)}{\cos(\gamma)^3} \cdot c_i^{(\mathrm{I},2)} \sin(i\gamma) \right\}, \\
h_{12}(\gamma) &= \sum_{i=1}^{6} \left\{ 2\tan(\gamma) \cdot c_i^{(\mathrm{I},1)} \cos[(i-1)\gamma] + \frac{1}{\cos(\gamma)^2} \cdot c_i^{(\mathrm{I},2)} \sin(i\gamma) \right\}, \\
h_{21}(\gamma) &= \sum_{i=1}^{6} \left\{ \left[1-\tan(\gamma)^2\right] \cdot c_i^{(\mathrm{II},1)} \sin(i\gamma) - \frac{\tan(\gamma)}{\cos(\gamma)^2} \cdot c_i^{(\mathrm{II},2)} \cos[(i-1)\gamma] \right\}, \\
h_{22}(\gamma) &= \sum_{i=1}^{6} \left\{ 2\tan(\gamma) \cdot c_i^{(\mathrm{II},1)} \sin(i\gamma) + \frac{1}{\cos(\gamma)^2} \cdot c_i^{(\mathrm{II},2)} \cos[(i-1)\gamma] \right\},
\end{aligned}
, \tag{29}
$$

where $c_i^{(\mathrm{I},1)}$, $c_i^{(\mathrm{II},1)}$, $c_i^{(\mathrm{I},2)}$, and $c_i^{(\mathrm{II},2)}$ are given by the following Table 1.

As cracks are assumed to nucleate perpendicularly to the structural boundary, the angle γ is set to 0, which leads to a simplified $\boldsymbol{H}(\gamma)$ matrix:

$$
\boldsymbol{H}(0) = \sum_{i=1}^{6} \begin{bmatrix} c_i^{(\mathrm{I},1)} & 0 \\ 0 & c_i^{(\mathrm{II},2)} \end{bmatrix}. \tag{30}
$$

Appendix B. Energy release rate coordinate transformation

The energy release rate was given in Eqs. (21) and (22) both in polar and Cartesian coordinates, respectively. In fact, expanding the matrix $\boldsymbol{Q}(\gamma, \beta)$, the expression for the energy release rate takes the form

$$
G(\boldsymbol{x}_i, \eta, \gamma, \beta) = \frac{\pi\eta}{E_1} \boldsymbol{\sigma}(\boldsymbol{x}_i)^{\mathsf{T}} \boldsymbol{Q}(\gamma, \beta) \boldsymbol{\sigma}(\boldsymbol{x}_i) = \frac{\pi\eta}{E_1} \boldsymbol{\sigma}(\boldsymbol{x}_i)^{\mathsf{T}} \boldsymbol{P}_g(\beta)^{\mathsf{T}} \boldsymbol{P}_l(\gamma)^{\mathsf{T}} \boldsymbol{H}^{\mathsf{T}}(\gamma) \boldsymbol{H}(\gamma) \boldsymbol{P}_l(\gamma) \boldsymbol{P}_g(\beta) \boldsymbol{\sigma}(\boldsymbol{x}_i), \tag{31}
$$

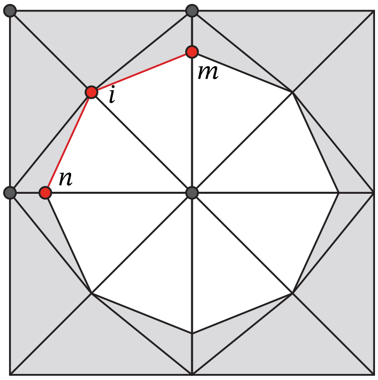

Fig. 20. Line elements ni and im (marked with red segments) sharing node i are used to compute the outward normal $\boldsymbol{n}_i$ of node i.

where we assume that cracks always nucleate perpendicularly to the boundary, *i.e.*, $\gamma = 0$ then for all potential cracks. $\boldsymbol{P}_g(\beta)$ is a 4 × 4 matrix defined as

$$\begin{aligned}\boldsymbol{P}_g(\beta) &= \begin{bmatrix} \cos^2\beta & \sin\beta\cos\beta & \sin\beta\cos\beta & \sin^2\beta \\ -\sin\beta\cos\beta & \cos^2\beta & -\sin^2\beta & \sin\beta\cos\beta \\ -\sin\beta\cos\beta & -\sin^2\beta & \cos^2\beta & \sin\beta\cos\beta \\ \sin^2\beta & -\sin\beta\cos\beta & -\sin\beta\cos\beta & \cos^2\beta \end{bmatrix} \\ &= \begin{bmatrix} n_x^2 & n_x n_y & n_x n_y & n_y^2 \\ -n_x n_y & n_x^2 & -n_y^2 & n_x n_y \\ -n_x n_y & -n_y^2 & n_x^2 & n_x n_y \\ n_y^2 & -n_x n_y & -n_x n_y & n_x^2 \end{bmatrix}. \end{aligned} \tag{32}$$

where $\boldsymbol{n} = (n_x, n_y) = (-\cos\beta, -\sin\beta)$ is the outward normal of the local boundary.

Under the discretized model, $\boldsymbol{n}$ is expressed as the outward normal $\boldsymbol{n}_i$ of node i that is evaluated by averaging the normal of segments along material interfaces. As shown in Fig. 20, node i is shared by two line elements ni and im (marked with red segments). The average of normals of these two segments is evaluated as

$$\boldsymbol{n}_{\text{avg}} = (n_{\text{avg}x}, n_{\text{avg}y}) = \frac{1}{2}\left(\boldsymbol{n}_{ni} + \boldsymbol{n}_{im}\right). \tag{33}$$

Then $\boldsymbol{n}_i$ is evaluated by normalizing $\boldsymbol{n}_{\text{avg}}$ as

$$\boldsymbol{n}_i = (n_x, n_y) = \frac{(n_{\text{avg}x}, n_{\text{avg}y})}{\sqrt{n_{\text{avg}x}^2 + n_{\text{avg}y}^2}}. \tag{34}$$

The other transformation matrix $\boldsymbol{P}_l(\gamma)$ is given by

$$\boldsymbol{P}_l(\gamma) = \begin{bmatrix} \sin^2(\gamma) & -\frac{\sin(2\gamma)}{2} & -\frac{\sin(2\gamma)}{2} & \cos^2(\gamma) \\ -\sin(\gamma)\cos(\gamma) & \frac{\cos^2(\gamma)-\sin^2(\gamma)}{2} & \frac{\cos^2(\gamma)-\sin^2(\gamma)}{2} & \sin(\gamma)\cos(\gamma) \end{bmatrix}. \tag{35}$$

Setting the angle $\gamma = 0$, $\boldsymbol{P}_l(\gamma)$ is simplified to

$$\boldsymbol{P}_l(0) = \begin{bmatrix} 0 & 0 & 0 & 1 \\ 0 & 0.5 & 0.5 & 0 \end{bmatrix}. \tag{36}$$

Appendix C. Interpolation matrices and differential operator

The expressions for the interpolation matrices and for the differential operator used in the proposed stress recovery technique are:

$$\boldsymbol{E}_\sigma = \begin{bmatrix} 1 & x & y & xy & x^2 & y^2 & 0 & 0 & 0 & 0 & 0 & 0 & 0 & 0 & 0 & 0 & 0 & 0 \\ 0 & 0 & 0 & 0 & 0 & 0 & 1 & x & y & xy & x^2 & y^2 & 0 & 0 & 0 & 0 & 0 & 0 \\ 0 & 0 & 0 & 0 & 0 & 0 & 0 & 0 & 0 & 0 & 0 & 0 & 1 & x & y & xy & x^2 & y^2 \end{bmatrix}, \tag{37}$$

$$\bar{\boldsymbol{E}}_\sigma = \begin{bmatrix} 1 & 0 & 0 & x & y & 2xy & 0 & 0 & 0 & y^2 & 0 & x^2 \\ 0 & 1 & 0 & 0 & 0 & 0 & x & z & 2xy & 0 & x^2 & y^2 \\ 0 & 0 & 1 & -y & 0 & -y^2 & 0 & -x & -x^2 & 0 & 0 & -2xy \end{bmatrix}, \tag{38}$$

$$\boldsymbol{E}_\zeta = \begin{bmatrix} 1 & x & y & 0 & 0 & 0 \\ 0 & 0 & 0 & 1 & x & y \end{bmatrix}, \tag{39}$$

$$\boldsymbol{\partial}_\sigma = \begin{bmatrix} \frac{\partial}{\partial x} & 0 & \frac{\partial}{\partial y} \\ 0 & \frac{\partial}{\partial y} & \frac{\partial}{\partial x} \end{bmatrix}. \tag{40}$$

Appendix D. Detailed sensitivity formulation

D.1. $\frac{\partial J}{\partial s_j}$ And $\frac{\partial J}{\partial \tilde{\boldsymbol{U}}}$

According to Eq. (15), the derivative of J with respect to design variable s_j is expressed as

$$\frac{\partial J}{\partial s_j} = \left(\frac{1}{N_{\text{node}}}\right)^{\frac{1}{p}} \frac{1}{p} \left(\sum_{i=1}^{N_{\text{node}}} G_i^p\right)^{\frac{1}{p}-1} \left(\sum_{i=1}^{N_{\text{node}}} p G_i^{p-1} \frac{\partial G_i}{\partial s_j}\right), \tag{41}$$

where

$$\begin{aligned} \frac{\partial G_i}{\partial s_j} &= \frac{\pi \eta}{\overline{E}_1} \frac{\partial \left(\boldsymbol{\sigma}(\boldsymbol{x}_i)^\mathsf{T} \boldsymbol{Q}(\gamma, \beta) \boldsymbol{\sigma}(\boldsymbol{x}_i)\right)}{\partial s_j} \\ &= \frac{\pi \eta}{\overline{E}_1} \left(\frac{\partial \boldsymbol{\sigma}(\boldsymbol{x}_i)^\mathsf{T}}{\partial s_j} \boldsymbol{Q}(\gamma, \beta) \boldsymbol{\sigma}(\boldsymbol{x}_i) + \boldsymbol{\sigma}(\boldsymbol{x}_i)^\mathsf{T} \frac{\partial \boldsymbol{Q}(\gamma, \beta)}{\partial s_j} \boldsymbol{\sigma}(\boldsymbol{x}_i) + \boldsymbol{\sigma}(\boldsymbol{x}_i)^\mathsf{T} \boldsymbol{Q}(\gamma, \beta) \frac{\partial \boldsymbol{\sigma}(\boldsymbol{x}_i)}{\partial s_j} \right). \end{aligned} \tag{42}$$

According to Eq. (24), the derivative of nodal stress $\boldsymbol{\sigma}(\boldsymbol{x}_i)$ with respect to design variable s_j is defined as

$$\frac{\partial \boldsymbol{\sigma}(\boldsymbol{x}_i)}{\partial s_j} = \frac{\partial \boldsymbol{\sigma}(\boldsymbol{x}_i)}{\partial \boldsymbol{x}_n} \frac{\partial \boldsymbol{x}_n}{\partial s_j} = \frac{1}{N_i} \frac{\partial \left(\sum \boldsymbol{E}_\sigma(\boldsymbol{x}_i) \hat{\boldsymbol{\sigma}}_e\right)}{\partial \boldsymbol{x}_n} \frac{\partial \boldsymbol{x}_n}{\partial s_j} = \frac{1}{N_i} \sum \left(\frac{\partial \boldsymbol{E}_\sigma(\boldsymbol{x}_i)}{\partial \boldsymbol{x}_n} \hat{\boldsymbol{\sigma}}_e + \boldsymbol{E}_\sigma(\boldsymbol{x}_i) \frac{\partial \hat{\boldsymbol{\sigma}}_e}{\partial \boldsymbol{x}_n} \right) \frac{\partial \boldsymbol{x}_n}{\partial s_j}. \tag{43}$$

The first term $(\partial \boldsymbol{E}_\sigma(\boldsymbol{x}_i)/\partial \boldsymbol{x}_n) \hat{\boldsymbol{\sigma}}_e$ is only non-zero, when $\boldsymbol{x}_i$ equals enriched node $\boldsymbol{x}_n$, and derivatives of $\boldsymbol{E}_\sigma(\boldsymbol{x}_i)$ with respect to coordinates (x_i, y_i) are given by

$$\begin{aligned} \frac{\partial \boldsymbol{E}_\sigma(\boldsymbol{x}_i)}{\partial x_i} &= \begin{bmatrix} 0 & 1 & 0 & y_i & 2x_i & 0 & 0 & 0 & 0 & 0 & 0 & 0 & 0 & 0 & 0 & 0 & 0 & 0 \\ 0 & 0 & 0 & 0 & 0 & 0 & 0 & 1 & 0 & y_i & 2x_i & 0 & 0 & 0 & 0 & 0 & 0 & 0 \\ 0 & 0 & 0 & 0 & 0 & 0 & 0 & 0 & 0 & 0 & 0 & 0 & 0 & 1 & 0 & y_i & 2x_i & 0 \end{bmatrix}, \\ \frac{\partial \boldsymbol{E}_\sigma(\boldsymbol{x}_i)}{\partial y_i} &= \begin{bmatrix} 0 & 0 & 1 & x_i & 0 & 2y_i & 0 & 0 & 0 & 0 & 0 & 0 & 0 & 0 & 0 & 0 & 0 & 0 \\ 0 & 0 & 0 & 0 & 0 & 0 & 0 & 0 & 1 & x_i & 0 & 2y_i & 0 & 0 & 0 & 0 & 0 & 0 \\ 0 & 0 & 0 & 0 & 0 & 0 & 0 & 0 & 0 & 0 & 0 & 0 & 0 & 0 & 1 & x_i & 0 & 2y_i \end{bmatrix}. \end{aligned} \tag{44}$$

In order to evaluate $\partial \hat{\boldsymbol{\sigma}}_e / \partial \boldsymbol{x}_n$, we need to solve the derivative of Eq. (23), which is used to obtain the recovered stress field. For simplicity, we redefine several terms in Eq. (23) as

$$\boldsymbol{A}_e = \begin{bmatrix} \int_e \bar{\boldsymbol{E}}_\sigma^\mathsf{T} \boldsymbol{E}_\sigma \mathrm{d}e \\ \int_e \boldsymbol{E}_\zeta^\mathsf{T} \partial_\sigma \boldsymbol{E}_\sigma \mathrm{d}e \end{bmatrix}, \boldsymbol{B}_{e1} = \int_e \bar{\boldsymbol{E}}_\sigma^\mathsf{T} \boldsymbol{\sigma}_e^h \mathrm{d}e, \boldsymbol{B}_{e2} = \int_e \boldsymbol{E}_\zeta^\mathsf{T} \boldsymbol{b} \mathrm{d}e. \tag{45}$$

Then, the corresponding derivative associated with enriched node $\boldsymbol{x}_n$ is given by

$$\left(\sum_{\{e \in \mathcal{E}_i\}} \frac{\partial \boldsymbol{A}_e}{\partial \boldsymbol{x}_n}\right) \hat{\boldsymbol{\sigma}}_e + \left(\sum_{\{e \in \mathcal{E}_i\}} \boldsymbol{A}_e\right) \frac{\partial \hat{\boldsymbol{\sigma}}_e}{\partial \boldsymbol{x}_n} = \sum_{\{e \in \mathcal{E}_i\}} \begin{bmatrix} \frac{\partial \boldsymbol{B}_{e1}}{\partial \boldsymbol{x}_n} \\ \frac{\partial \boldsymbol{B}_{e2}}{\partial \boldsymbol{x}_n} \end{bmatrix}. \tag{46}$$

After solving Eq. (46), the derivative of $\hat{\boldsymbol{\sigma}}_e$ with respect to enriched node $\boldsymbol{x}_n$ is expressed as

$$\frac{\partial \hat{\boldsymbol{\sigma}}_e}{\partial \boldsymbol{x}_n} = \left(\sum_{\{e \in \mathcal{E}_i\}} \boldsymbol{A}_e\right)^{-1} \left(\sum_{\{e \in \mathcal{E}_i\}} \begin{bmatrix} \frac{\partial \boldsymbol{B}_{e1}}{\partial \boldsymbol{x}_n} \\ \frac{\partial \boldsymbol{B}_{e2}}{\partial \boldsymbol{x}_n} \end{bmatrix} - \left(\sum_{\{e \in \mathcal{E}_i\}} \frac{\partial \boldsymbol{A}_e}{\partial \boldsymbol{x}_n}\right) \hat{\boldsymbol{\sigma}}_e\right). \tag{47}$$

According to Appendix C and Eq. (45), $\partial \boldsymbol{A}_e / \partial \boldsymbol{x}_n$ and $\partial \boldsymbol{B}_{ei} / \partial \boldsymbol{x}_n, i = 1, 2$ can be obtained directly. As enriched nodes are created at intersections between element edges and material interfaces, their locations are evaluated based on level set values and coordinates of background mesh nodes. As shown in Fig. 21, enriched node $\boldsymbol{x}_n$ is related to original mesh nodes $\boldsymbol{x}_k$ and $\boldsymbol{x}_l$ as

$$\boldsymbol{x}_n = \boldsymbol{x}_l - \frac{\phi_l}{\phi_k - \phi_l} \left(\boldsymbol{x}_k - \boldsymbol{x}_l \right), \tag{48}$$

where ϕ_k and ϕ_l are level set values of $\boldsymbol{x}_k$ and $\boldsymbol{x}_l$, respectively. The derivative of $\boldsymbol{x}_n$ with respect to design variable s_j is then given by

$$\frac{\partial \boldsymbol{x}_n}{\partial s_j} = \frac{\partial \boldsymbol{x}_n}{\partial \phi_l} \frac{\partial \phi_l}{\partial s_j} + \frac{\partial \boldsymbol{x}_n}{\partial \phi_k} \frac{\partial \phi_k}{\partial s_j}, \tag{49}$$

where

$$\frac{\partial \boldsymbol{x}_n}{\partial \phi_l} = -\frac{\phi_k}{\left(\phi_k - \phi_l \right)^2} \left(\boldsymbol{x}_k - \boldsymbol{x}_l \right), \tag{50}$$

and

$$\frac{\partial \boldsymbol{x}_n}{\partial \phi_k} = -\frac{\phi_l}{\left(\phi_k - \phi_l \right)^2} \left(\boldsymbol{x}_k - \boldsymbol{x}_l \right). \tag{51}$$

Since the level set function ϕ is discretized by means of compactly supported RBFs (see Eq. (17) and Fig. 4), $\partial \phi_l / \partial s_j = \zeta_j(\boldsymbol{x}_l)$ and $\partial \phi_k / \partial s_j = \zeta_j(\boldsymbol{x}_k)$. The derivative of $\boldsymbol{Q}(\gamma, \beta)$ with respect to design variable s_j in Eq. (42) is given in Appendix E. The derivative of J with respect to the displacement $\tilde{\boldsymbol{U}}$ is

$$\frac{\partial J}{\partial \tilde{\boldsymbol{U}}} = \left(\frac{1}{N_{\text{node}}} \right)^{\frac{1}{p}} \frac{1}{p} \left(\sum_{i=1}^{N_{\text{node}}} G_i^p \right)^{\frac{1}{p}-1} \left(\sum_{i=1}^{N_{\text{node}}} p G_i^{p-1} \frac{\partial G_i}{\partial \tilde{\boldsymbol{U}}} \right), \tag{52}$$

where

$$\frac{\partial G_i}{\partial \tilde{\boldsymbol{U}}} = \frac{\pi \varepsilon}{\overline{E}_1} \frac{\partial \left(\boldsymbol{\sigma}(\boldsymbol{x}_i)^{\intercal} \boldsymbol{Q}(\gamma, \beta) \boldsymbol{\sigma}(\boldsymbol{x}_i) \right)}{\partial \tilde{\boldsymbol{U}}} = \frac{\pi \varepsilon}{\overline{E}_1} \left(\frac{\partial \boldsymbol{\sigma}(\boldsymbol{x}_i)^{\intercal}}{\partial \tilde{\boldsymbol{U}}} \boldsymbol{Q}(\gamma, \beta) \boldsymbol{\sigma}(\boldsymbol{x}_i) + \boldsymbol{\sigma}(\boldsymbol{x}_i)^{\intercal} \boldsymbol{Q}(\gamma, \beta) \frac{\partial \boldsymbol{\sigma}(\boldsymbol{x}_i)}{\partial \tilde{\boldsymbol{U}}} \right). \tag{53}$$

Similar to Eq. (43), the derivative of $\boldsymbol{\sigma}(\boldsymbol{x}_i)$ with respect to displacement $\tilde{\boldsymbol{U}}$ is given by

$$\frac{\partial \boldsymbol{\sigma}(\boldsymbol{x}_i)}{\partial \tilde{\boldsymbol{U}}} = \frac{\partial \left(\sum \boldsymbol{E}_{\sigma}(\boldsymbol{x}_i) \hat{\boldsymbol{\sigma}}_e \right)}{\partial \tilde{\boldsymbol{U}}} = \sum \left(\frac{\partial \boldsymbol{E}_{\sigma}(\boldsymbol{x}_i)}{\partial \tilde{\boldsymbol{U}}} \hat{\boldsymbol{\sigma}}_e + \boldsymbol{E}_{\sigma}(\boldsymbol{x}_i) \frac{\partial \hat{\boldsymbol{\sigma}}_e}{\partial \tilde{\boldsymbol{U}}} \right) = \sum \left(\boldsymbol{E}_{\sigma}(\boldsymbol{x}_i) \frac{\partial \hat{\boldsymbol{\sigma}}_e}{\partial \tilde{\boldsymbol{U}}} \right) = \boldsymbol{E}_{\sigma}(\boldsymbol{x}_i) \sum \frac{\partial \hat{\boldsymbol{\sigma}}_e}{\partial \tilde{\boldsymbol{U}}}. \tag{54}$$

In order to evaluate $\partial \hat{\boldsymbol{\sigma}}_e / \partial \tilde{\boldsymbol{U}}$, we need to solve the derivative of Eq. (23) with respect to $\tilde{\boldsymbol{U}}$. Then, the corresponding derivative is expressed as

$$\frac{\partial \hat{\boldsymbol{\sigma}}_e}{\partial \tilde{\boldsymbol{U}}} = \left(\sum_{\{e \in \mathcal{E}_i\}} \boldsymbol{A}_e \right)^{-1} \left(\sum_{\{e \in \mathcal{E}_i\}} \begin{bmatrix} \frac{\partial \boldsymbol{B}_{e1}}{\partial \tilde{\boldsymbol{U}}} \\ \frac{\partial \boldsymbol{B}_{e2}}{\partial \tilde{\boldsymbol{U}}} \end{bmatrix} - \left(\sum_{\{e \in \mathcal{E}_i\}} \frac{\partial \boldsymbol{A}_e}{\partial \tilde{\boldsymbol{U}}} \right) \hat{\boldsymbol{\sigma}}_e \right). \tag{55}$$

As shown in Eq. (45), $\boldsymbol{A}_e$ is only related to coordinates, so $\partial \boldsymbol{A}_e / \partial \tilde{\boldsymbol{U}} = \boldsymbol{0}$.

D.2. $\frac{\partial \tilde{\boldsymbol{K}}}{\partial s_j}$ *And* $\frac{\partial \tilde{\boldsymbol{F}}}{\partial s_j}$

According to Eq. (13), derivatives of $\tilde{\boldsymbol{K}}$ and $\tilde{\boldsymbol{F}}$ with respect to design variable s_j are expressed as

$$\frac{\partial \tilde{\boldsymbol{K}}}{\partial s_j} = \frac{\partial \boldsymbol{T}^{\intercal}}{\partial s_j} \boldsymbol{K} \boldsymbol{T} \tilde{\boldsymbol{U}} + \boldsymbol{T}^{\intercal} \frac{\partial \boldsymbol{K}}{\partial s_j} \boldsymbol{T} \tilde{\boldsymbol{U}} + \boldsymbol{T}^{\intercal} \boldsymbol{K} \frac{\partial \boldsymbol{T}}{\partial s_j} \tilde{\boldsymbol{U}}, \tag{56}$$

and

$$\frac{\partial \tilde{\boldsymbol{F}}}{\partial s_j} = \frac{\partial \boldsymbol{T}^{\intercal}}{\partial s_j} (\boldsymbol{F} - \boldsymbol{K} \boldsymbol{g}) + \boldsymbol{T}^{\intercal} \left(\frac{\partial \boldsymbol{F}}{\partial s_j} - \frac{\partial \boldsymbol{K}}{\partial s_j} \boldsymbol{g} - \boldsymbol{K} \frac{\partial \boldsymbol{g}}{\partial s_j} \right). \tag{57}$$

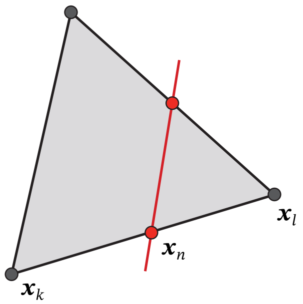

Fig. 21. Enriched nodes $\boldsymbol{x}_n$ is created at the intersection between a material interface (marked in red) and an element edge with nodes $\boldsymbol{x}_k$ and $\boldsymbol{x}_l$.

According to Eqs. (7) and (9), $\partial \boldsymbol{K}/\partial s_j$ and $\partial \boldsymbol{F}/\partial s_j$ can be evaluated directly. $\partial \boldsymbol{g}/\partial s_j$ is a zero vector as prescribed displacements are not related to design variables in this paper. As shown in Eq. (12), the transformation matrix $\boldsymbol{T}$ is constructed with shape function $N_i, i = 1, 2, 3$, so it can be expressed as a 10×10 matrix:

$$\boldsymbol{T} = \left[\begin{array}{cccccc:cccc} 1 & 0 & 0 & 0 & 0 & 0 & 0 & 0 & 0 & 0 \\ 0 & 1 & 0 & 0 & 0 & 0 & 0 & 0 & 0 & 0 \\ 0 & 0 & 1 & 0 & 0 & 0 & 0 & 0 & 0 & 0 \\ 0 & 0 & 0 & 1 & 0 & 0 & 0 & 0 & 0 & 0 \\ 0 & 0 & 0 & 0 & 1 & 0 & 0 & 0 & 0 & 0 \\ 0 & 0 & 0 & 0 & 0 & 1 & 0 & 0 & 0 & 0 \\ \hdashline -N_1 & 0 & -N_2 & 0 & 0 & 0 & 1 & 0 & 0 & 0 \\ 0 & -N_1 & 0 & -N_2 & 0 & 0 & 0 & 1 & 0 & 0 \\ 0 & 0 & -N_2 & 0 & -N_3 & 0 & 0 & 0 & 1 & 0 \\ 0 & 0 & 0 & -N_2 & 0 & -N_3 & 0 & 0 & 0 & 1 \end{array}\right]. \tag{58}$$

Its sensitivity with respect to design variable s_j can be computed as

$$\frac{\partial \boldsymbol{T}}{\partial s_j} = \left[\begin{array}{cccccc:cccc} 1 & 0 & 0 & 0 & 0 & 0 & 0 & 0 & 0 & 0 \\ 0 & 1 & 0 & 0 & 0 & 0 & 0 & 0 & 0 & 0 \\ 0 & 0 & 1 & 0 & 0 & 0 & 0 & 0 & 0 & 0 \\ 0 & 0 & 0 & 1 & 0 & 0 & 0 & 0 & 0 & 0 \\ 0 & 0 & 0 & 0 & 1 & 0 & 0 & 0 & 0 & 0 \\ 0 & 0 & 0 & 0 & 0 & 1 & 0 & 0 & 0 & 0 \\ \hdashline -\frac{\partial N_1}{\partial s_j} & 0 & -\frac{\partial N_2}{\partial s_j} & 0 & 0 & 0 & 0 & 0 & 0 & 0 \\ 0 & -\frac{\partial N_1}{\partial s_j} & 0 & -\frac{\partial N_2}{\partial s_j} & 0 & 0 & 0 & 0 & 0 & 0 \\ 0 & 0 & -\frac{\partial N_2}{\partial s_j} & 0 & -\frac{\partial N_3}{\partial s_j} & 0 & 0 & 0 & 0 & 0 \\ 0 & 0 & 0 & -\frac{\partial N_2}{\partial s_j} & 0 & -\frac{\partial N_3}{\partial s_j} & 0 & 0 & 0 & 0 \end{array}\right], \tag{59}$$

where the derivative of shape function $N_i, i = 1, 2, 3$ with respect to design variable s_j is explained in detail in Ref. [57].

D.3. $\frac{\partial J_{\sigma_{vM}}}{\partial s_j}$, *and* $\frac{\partial J_{\sigma_{vM}}}{\partial \tilde{\boldsymbol{U}}}$

Considering the objective function $J_{\sigma_{\mathrm{vM}}}$ associated with von Mises stress, it is given by

$$J_{\sigma_{\mathrm{vM}}} = \frac{1}{N_{\mathrm{e}}} \sum_{i=1}^{N_{\mathrm{e}}} (\sigma_{\mathrm{vM}i} - \bar{\sigma}_{\mathrm{vM}})^q \,. \tag{60}$$

Its derivative associated to design variable s_j is then given by

$$\frac{\partial J_{\sigma_{\text{vM}}}}{\partial s_j} = \frac{q}{N_{\text{e}}} \sum_{i=1}^{N_{\text{e}}} \left(\left(\sigma_{\text{vM}i} - \bar{\sigma}_{\text{vM}}\right)^{q-1} \frac{\partial \left(\sigma_{\text{vM}i} - \bar{\sigma}_{\text{vM}}\right)}{\partial s_j} \right) = \frac{q}{N_{\text{e}}} \sum_{i=1}^{N_{\text{e}}} \left(\left(\sigma_{\text{vM}i} - \bar{\sigma}_{\text{vM}}\right)^{q-1} \frac{\partial \left(\sigma_{\text{vM}i} - \bar{\sigma}_{\text{vM}}\right)}{\partial \boldsymbol{x}_n} \frac{\partial \boldsymbol{x}_n}{\partial s_j} \right). \tag{61}$$

As von Mises stress σ_{vM} in 2D is expressed as

$$\sigma_{\text{vM}} = \sqrt{\sigma_{xx}^2 + \sigma_{yy}^2 - \sigma_{xx}\sigma_{yy} + 3\sigma_{xy}^2} = \sqrt{\boldsymbol{\sigma}^{\intercal} \boldsymbol{R} \boldsymbol{\sigma}}, \tag{62}$$

where

$$\boldsymbol{R} = \begin{bmatrix} 1 & 0 & 0 & -0.5 \\ 0 & 1 & 0.5 & 0 \\ 0 & 0.5 & 1 & 0 \\ -0.5 & 0 & 0 & 1 \end{bmatrix}, \tag{63}$$

its derivative with respect to design variable s_j is

$$\frac{\partial \sigma_{\text{vM}}}{\partial s_j} = \frac{\partial \sqrt{\boldsymbol{\sigma}^{\intercal} \boldsymbol{R} \boldsymbol{\sigma}}}{\partial s_j} = \frac{1}{2\sigma_{\text{vM}}} \left(\frac{\partial \boldsymbol{\sigma}^{\intercal}}{\partial s_j} \boldsymbol{R} \boldsymbol{\sigma} + \boldsymbol{\sigma}^{\intercal} \boldsymbol{R} \frac{\partial \boldsymbol{\sigma}}{\partial s_j} \right). \tag{64}$$

Then the sensitivity term $\left(\partial \left(\sigma_{\text{vM}i} - \bar{\sigma}_{\text{vM}}\right)\right) / \partial s_j$ in Eq. (61) is expressed as

$$\frac{\partial \left(\sigma_{\text{vM}i} - \bar{\sigma}_{\text{vM}}\right)}{\partial s_j} = \frac{1}{2\sigma_{\text{vM}i}} \left(\frac{\partial \boldsymbol{\sigma}_i^{\intercal}}{\partial s_j} \boldsymbol{R} \boldsymbol{\sigma}_i + \boldsymbol{\sigma}_i^{\intercal} \boldsymbol{R} \frac{\partial \boldsymbol{\sigma}_i}{\partial s_j} \right) - \frac{1}{N_e} \sum_{l=1}^{N_{\text{e}}} \frac{\partial \sigma_{\text{vM}l}}{\partial s_j}. \tag{65}$$

The derivative of the recovered element stress $\boldsymbol{\sigma}_i$ with respect to design variable s_j is given by

$$\frac{\partial \boldsymbol{\sigma}_i}{\partial s_j} = \frac{\partial \left(\boldsymbol{E}_{\sigma}(\boldsymbol{x}_g) \hat{\boldsymbol{\sigma}}_i \right)}{\partial s_j} = \left(\frac{\partial \boldsymbol{E}_{\sigma}(\boldsymbol{x}_g)}{\partial \boldsymbol{x}_n} \hat{\boldsymbol{\sigma}}_i + \boldsymbol{E}_{\sigma}(\boldsymbol{x}_g) \frac{\partial \hat{\boldsymbol{\sigma}}_i}{\partial \boldsymbol{x}_n} \right) \frac{\partial \boldsymbol{x}_n}{\partial s_j}, \tag{66}$$

where $\boldsymbol{x}_g$ is the global coordinate of gauss points in the ith element, $\partial \hat{\boldsymbol{\sigma}}_i / \partial \boldsymbol{x}_n$ can be obtained by solving Eq. (47), and $\hat{\boldsymbol{\sigma}}_i$ is a vector derived from Eq. (23). The derivative of interpolation matrix $\boldsymbol{E}_{\sigma}(\boldsymbol{x}_g)$ associated to $\boldsymbol{x}_n$ is defined as

$$\frac{\partial \boldsymbol{E}_{\sigma}(\boldsymbol{x}_g)}{\partial \boldsymbol{x}_n} = \frac{\partial \boldsymbol{E}_{\sigma}(\boldsymbol{x}_g)}{\partial \boldsymbol{x}_g} \frac{\partial \boldsymbol{x}_g}{\partial \boldsymbol{x}_n} = \frac{\partial \boldsymbol{E}_{\sigma}(\boldsymbol{x}_g)}{\partial \boldsymbol{x}_g} \frac{\partial \boldsymbol{X}_e^{\intercal}}{\partial \boldsymbol{x}_n} \begin{bmatrix} \boldsymbol{N}(\boldsymbol{\xi}_i) \\ \boldsymbol{\psi}(\boldsymbol{\xi}_i) \end{bmatrix}, \tag{67}$$

where $\boldsymbol{X}_e$ are the nodal coordinates of the ith element, and $\boldsymbol{\xi}_i$ is the local coordinate of Gauss point.

The derivative of $J_{\sigma_{\text{vM}}}$ with respect to the displacement $\tilde{\boldsymbol{U}}$ is

$$\frac{\partial J_{\sigma_{\text{vM}}}}{\partial \tilde{\boldsymbol{U}}} = \frac{q}{N_{\text{e}}} \sum_{i=1}^{N_e} \left(\left(\sigma_{\text{vM}i} - \bar{\sigma}_{\text{vM}}\right)^{q-1} \frac{\partial \left(\sigma_{\text{vM}i} - \bar{\sigma}_{\text{vM}}\right)}{\partial \tilde{\boldsymbol{U}}} \right), \tag{68}$$

where

$$\frac{\partial \left(\sigma_{\text{vM}i} - \bar{\sigma}_{\text{vM}}\right)}{\partial \tilde{\boldsymbol{U}}} = \frac{1}{2\sigma_{\text{vM}i}} \left(\frac{\partial \boldsymbol{\sigma}_i^{\intercal}}{\partial \tilde{\boldsymbol{U}}} \boldsymbol{R} \boldsymbol{\sigma}_i + \boldsymbol{\sigma}_i^{\intercal} \boldsymbol{R} \frac{\partial \boldsymbol{\sigma}_i}{\partial \tilde{\boldsymbol{U}}} \right) - \frac{1}{N_e} \sum_{l=1}^{N_{\text{e}}} \frac{\partial \sigma_{\text{vM}l}}{\partial \tilde{\boldsymbol{U}}}. \tag{69}$$

The derivative of the recovered element stress $\boldsymbol{\sigma}_i$ with respect to the displacement $\tilde{\boldsymbol{U}}$ is defined as

$$\frac{\partial \boldsymbol{\sigma}_i}{\partial \tilde{\boldsymbol{U}}} = \frac{\partial \left(\boldsymbol{E}_{\sigma}(\boldsymbol{x}_g) \hat{\boldsymbol{\sigma}}_i \right)}{\partial \tilde{\boldsymbol{U}}} = \frac{\partial \boldsymbol{E}_{\sigma}(\boldsymbol{x}_g)}{\partial \tilde{\boldsymbol{U}}} \hat{\boldsymbol{\sigma}}_i + \boldsymbol{E}_{\sigma}(\boldsymbol{x}_g) \frac{\partial \hat{\boldsymbol{\sigma}}_i}{\partial \tilde{\boldsymbol{U}}} = \boldsymbol{E}_{\sigma}(\boldsymbol{x}_g) \frac{\partial \hat{\boldsymbol{\sigma}}_i}{\partial \tilde{\boldsymbol{U}}}, \tag{70}$$

where $\partial \hat{\boldsymbol{\sigma}}_i / \partial \tilde{\boldsymbol{U}}$ can be obtained by solving Eq. (55).

Appendix E. Derivative of $\boldsymbol{Q}(\gamma, \beta)$ with respect to design variable s_j

According to Eq. (31), $\boldsymbol{Q}(\gamma, \beta)$ is a matrix used to transform stress $\boldsymbol{\sigma}$ defined in the global Cartesian coordinates to stress $\boldsymbol{\sigma}_\theta$ in polar coordinates, and it is expressed as

$$\boldsymbol{Q}(\gamma, \beta) = \boldsymbol{P}_g(\beta)^\mathsf{T} \boldsymbol{P}_l(\gamma)^\mathsf{T} \boldsymbol{H}^\mathsf{T}(\gamma) \boldsymbol{H}(\gamma) \boldsymbol{P}_l(\gamma) \boldsymbol{P}_g(\beta). \tag{71}$$

Since cracks are assumed to nucleate perpendicularly to the structural boundary, $\gamma = 0$. This means that matrices $\boldsymbol{P}_l(\gamma)$ and $\boldsymbol{H}(\gamma)$ are not affected by design variables. The derivative of matrix $\boldsymbol{Q}(\gamma, \beta)$ with respect to design variable s_j is then expressed as

$$\frac{\partial \boldsymbol{Q}(\gamma, \beta)}{\partial s_j} = \frac{\partial \boldsymbol{P}_g(\beta)^\mathsf{T}}{\partial s_j} \boldsymbol{P}_l(\gamma)^\mathsf{T} \boldsymbol{H}^\mathsf{T}(\gamma) \boldsymbol{H}(\gamma) \boldsymbol{P}_l(\gamma) \boldsymbol{P}_g(\beta) + \boldsymbol{P}_g(\beta)^\mathsf{T} \boldsymbol{P}_l(\gamma)^\mathsf{T} \boldsymbol{H}^\mathsf{T}(\gamma) \boldsymbol{H}(\gamma) \boldsymbol{P}_l(\gamma) \frac{\partial \boldsymbol{P}_g(\beta)}{\partial s_j}. \tag{72}$$

According to Eq. (32), the derivative of $\boldsymbol{P}_g(\beta)$ with respect to design variable s_j is

$$\frac{\partial \boldsymbol{P}_g(\beta)}{\partial s_j} = \begin{bmatrix} 2n_x \frac{\partial n_x}{\partial s_j} & \frac{\partial n_x}{\partial s_j} n_y + n_x \frac{\partial n_y}{\partial s_j} & \frac{\partial n_x}{\partial s_j} n_y + n_x \frac{\partial n_y}{\partial s_j} & 2n_y \frac{\partial n_y}{\partial s_j} \\ -(\frac{\partial n_x}{\partial s_j} n_y + n_x \frac{\partial n_y}{\partial s_j}) & 2n_x \frac{\partial n_x}{\partial s_j} & -2n_y \frac{\partial n_y}{\partial s_j} & \frac{\partial n_x}{\partial s_j} n_y + n_x \frac{\partial n_y}{\partial s_j} \\ -(\frac{\partial n_x}{\partial s_j} n_y + n_x \frac{\partial n_y}{\partial s_j}) & -2n_y \frac{\partial n_y}{\partial s_j} & 2n_x \frac{\partial n_x}{\partial s_j} & \frac{\partial n_x}{\partial s_j} n_y + n_x \frac{\partial n_y}{\partial s_j} \\ 2n_y \frac{\partial n_y}{\partial s_j} & -(\frac{\partial n_x}{\partial s_j} n_y + n_x \frac{\partial n_y}{\partial s_j}) & -(\frac{\partial n_x}{\partial s_j} n_y + n_x \frac{\partial n_y}{\partial s_j}) & 2n_x \frac{\partial n_x}{\partial s_j} \end{bmatrix}. \tag{73}$$

As shown in Eq. (34), sensitivities of n_x and n_y associated with design variable s_j are calculated, respectively, as

$$\frac{\partial n_x}{\partial s_j} = \frac{\partial \frac{n_{\text{avg}x}}{\sqrt{n_{\text{avg}x}^2 + n_{\text{avg}y}^2}}}{\partial s_j} = \frac{n_{\text{avg}y}^2 \frac{\partial n_{\text{avg}x}}{\partial s_j} - n_{\text{avg}x} n_{\text{avg}y} \frac{\partial n_{\text{avg}y}}{\partial s_j}}{(n_{\text{avg}x}^2 + n_{\text{avg}y}^2)\sqrt{n_{\text{avg}x}^2 + n_{\text{avg}y}^2}}, \tag{74}$$

and

$$\frac{\partial n_y}{\partial s_j} = \frac{\partial \frac{n_{\text{avg}y}}{\sqrt{n_{\text{avg}x}^2 + n_{\text{avg}y}^2}}}{\partial s_j} = \frac{n_{\text{avg}x}^2 \frac{\partial n_{\text{avg}y}}{\partial s_j} - n_{\text{avg}x} n_{\text{avg}y} \frac{\partial n_{\text{avg}x}}{\partial s_j}}{(n_{\text{avg}x}^2 + n_{\text{avg}y}^2)\sqrt{n_{\text{avg}x}^2 + n_{\text{avg}y}^2}}. \tag{75}$$

As the average normal $(n_{\text{avg}x}, n_{\text{avg}y})$ is evaluated by the normal of segments sharing node i, we take segment im as an example to illustrate the procedure for obtaining the derivative of segment normal $\boldsymbol{n}_{im}$. Fig. 20 shows that segment im is defined by two enriched nodes $\boldsymbol{x}_i$ and $\boldsymbol{x}_m$, and its direction and normal then can be expressed, respectively, as

$$\boldsymbol{d}_{im} = \frac{\boldsymbol{x}_i - \boldsymbol{x}_m}{\sqrt{(\boldsymbol{x}_i - \boldsymbol{x}_m) \cdot (\boldsymbol{x}_i - \boldsymbol{x}_m)}} = (\boldsymbol{d}_{imx}, \boldsymbol{d}_{imy}), \tag{76}$$

and

$$\boldsymbol{n}_{im} = (-\boldsymbol{d}_{imy}, \boldsymbol{d}_{imx}). \tag{77}$$

Then the derivative of the direction $\boldsymbol{d}_{im}$ with respect to design variable s_j is given by

$$\frac{\partial \boldsymbol{d}_{im}}{\partial s_j} = \frac{\sqrt{(\boldsymbol{x}_i - \boldsymbol{x}_m) \cdot (\boldsymbol{x}_i - \boldsymbol{x}_m)} \cdot \left(\frac{\partial \boldsymbol{x}_i}{\partial s_j} - \frac{\partial \boldsymbol{x}_m}{\partial s_j}\right) - (\boldsymbol{x}_i - \boldsymbol{x}_m) \cdot \frac{(\frac{\partial \boldsymbol{x}_i}{\partial s_j} - \frac{\partial \boldsymbol{x}_m}{\partial s_j}) \cdot (\boldsymbol{x}_i - \boldsymbol{x}_m)}{\sqrt{(\boldsymbol{x}_i - \boldsymbol{x}_m) \cdot (\boldsymbol{x}_i - \boldsymbol{x}_m)}}}{(\boldsymbol{x}_i - \boldsymbol{x}_m) \cdot (\boldsymbol{x}_i - \boldsymbol{x}_m)} \tag{78}$$

where $\partial \boldsymbol{x}_i / \partial s_j$ and $\partial \boldsymbol{x}_m / \partial s_j$ are extracted from Eq. (49). The derivative of $\boldsymbol{n}_{im}$ with respect to s_j can be obtained via Eq. (77).

References

[1] Z. Wu, K. Ghosh, X. Qing, V. Karbhari, F.K. Chang, Structural health monitoring of composite repair patches in bridge rehabilitation, in: M. Tomizuka, C.B. Yun, V. Giurgiutiu (Eds.), Smart Structures and Materials 2006: Sensors and Smart Structures Technologies for Civil, Mechanical, and Aerospace Systems, Vol. 6174, International Society for Optics and Photonics, 2006, pp. 670–678.

[2] R. Brighenti, Patch repair design optimisation for fracture and fatigue improvements of cracked plates, Int. J. Solids Struct. 44 (3) (2007) 1115–1131.

[3] A. Klarbring, B. Torstenfelt, U. Edlund, P. Schmidt, K. Simonsson, H. Ansell, Minimizing crack energy release rate by topology optimization, Struct. Multidiscip. Optim. 58 (4) (2018) 1695–1703.

[4] M.P. Bendsoe, O. Sigmund, Topology Optimization: Theory, Methods, and Applications, Springer Science & Business Media, 2013.

[5] N.P. van Dijk, K. Maute, M. Langelaar, F. Van Keulen, Level-set methods for structural topology optimization: a review, Struct. Multidiscip. Optim. 48 (3) (2013) 437–472.

[6] O. Sigmund, K. Maute, Topology optimization approaches, Struct. Multidiscip. Optim. 48 (6) (2013) 1031–1055.

[7] W. Zhang, D. Li, P. Kang, X. Guo, S.K. Youn, Explicit topology optimization using IGA-based moving morphable void (MMV) approach, Comput. Methods Appl. Mech. Engrg. 360 (2020) 112685.

[8] C.B.W. Pedersen, P. Allinger, Industrial implementation and applications of topology optimization and future needs, in: M.P. Bendsøe, N. Olhoff, O. Sigmund (Eds.), IUTAM Symposium on Topological Design Optimization of Structures, Machines and Materials, 2006, pp. 229–238.

[9] J. Zhu, W. Zhang, L. Xia, Topology optimization in aircraft and aerospace structures design, Arch. Comput. Methods Eng. 23 (4) (2016) 595–622.

[10] S. Amstutz, A.A. Novotny, Topological optimization of structures subject to Von Mises stress constraints, Struct. Multidiscip. Optim. 41 (3) (2010) 407–420.

[11] W. Zhang, D. Li, J. Zhou, Z. Du, B. Li, X. Guo, A Moving Morphable Void (MMV)-based explicit approach for topology optimization considering stress constraints, Comput. Methods Appl. Mech. Engrg. 334 (2018) 381–413.

[12] Z. Fan, L. Xia, W. Lai, Q. Xia, T. Shi, Evolutionary topology optimization of continuum structures with stress constraints, Struct. Multidiscip. Optim. 59 (2) (2019) 647–658.

[13] W. Zhang, S. Jiang, C. Liu, D. Li, P. Kang, S.K. Youn, X. Guo, Stress-related topology optimization of shell structures using IGA/TSA-based moving morphable void (MMV) approach, Comput. Methods Appl. Mech. Engrg. 366 (2020) 113036.

[14] M. Bruggi, P. Duysinx, Topology optimization for minimum weight with compliance and stress constraints, Struct. Multidiscip. Optim. 46 (3) (2012) 369–384.

[15] Y. Luo, Z. Kang, Topology optimization of continuum structures with Drucker–Prager yield stress constraints, Comput. Struct. 90 (2012) 65–75.

[16] S.H. Jeong, S.H. Park, D.H. Choi, G.H. Yoon, Topology optimization considering static failure theories for ductile and brittle materials, Comput. Struct. 110 (2012) 116–132.

[17] R. Yang, C. Chen, Stress-based topology optimization, Struct. Optim. 12 (2–3) (1996) 98–105.

[18] P. Duysinx, M.P. Bendsøe, Topology optimization of continuum structures with local stress constraints, Internat. J. Numer. Methods Engrg. 43 (8) (1998) 1453–1478.

[19] G. Kreisselmeier, R. Steinhauser, Systematic control design by optimizing a vector performance index, IFAC Proc. Vol. 12 (7) (1979) 113–117.

[20] E. Holmberg, B. Torstenfelt, A. Klarbring, Stress constrained topology optimization, Struct. Multidiscip. Optim. 48 (1) (2013) 33–47.

[21] P. Duysinx, O. Sigmund, New developments in handling stress constraints in optimal material distribution, in: 7th AIAA/USAF/NASA/ISSMO Symposium on Multidisciplinary Analysis and Optimization, 1998, p. 4906.

[22] C. Le, J. Norato, T. Bruns, C. Ha, D. Tortorelli, Stress-based topology optimization for continua, Struct. Multidiscip. Optim. 41 (4) (2010) 605–620.

[23] J. París, F. Navarrina, I. Colominas, M. Casteleiro, Block aggregation of stress constraints in topology optimization of structures, Adv. Eng. Softw. 41 (3) (2010) 433–441.

[24] W.S. Zhang, X. Guo, M.Y. Wang, P. Wei, Optimal topology design of continuum structures with stress concentration alleviation via level set method, Internat. J. Numer. Methods Engrg. 93 (9) (2013) 942–959.

[25] C.E. Inglis, Stresses in a plate due to the presence of cracks and sharp corners, Trans. Inst. Nav. Archit. 55 (1913) 219–241.

[26] F.V. Senhora, O. Giraldo-Londono, I.F. Menezes, G.H. Paulino, Topology optimization with local stress constraints: a stress aggregation-free approach, Struct. Multidiscip. Optim. 62 (4) (2020) 1639–1668.

[27] G. Allaire, F. Jouve, Minimum stress optimal design with the level set method, Eng. Anal. Bound. Elem. 32 (11) (2008) 909–918.

[28] Q. Xia, T. Shi, S. Liu, M.Y. Wang, A level set solution to the stress-based structural shape and topology optimization, Comput. Struct. 90 (2012) 55–64.

[29] R. Picelli, S. Townsend, C. Brampton, J. Norato, H. Kim, Stress-based shape and topology optimization with the level set method, Comput. Methods Appl. Mech. Engrg. 329 (2018) 1–23.

[30] M.P. Bendsøe, A.R. Díaz, A method for treating damage related criteria in optimal topology design of continuum structures, Struct. Optim. 16 (2–3) (1998) 108–115.

[31] O. Amir, O. Sigmund, Reinforcement layout design for concrete structures based on continuum damage and truss topology optimization, Struct. Multidiscip. Optim. 47 (2) (2013) 157–174.

[32] O. Amir, A topology optimization procedure for reinforced concrete structures, Comput. Struct. 114 (2013) 46–58.

[33] K.A. James, H. Waisman, Failure mitigation in optimal topology design using a coupled nonlinear continuum damage model, Comput. Methods Appl. Mech. Engrg. 268 (2014) 614–631.

[34] K.A. James, H. Waisman, Topology optimization of structures under variable loading using a damage superposition approach, Internat. J. Numer. Methods Engrg. 101 (5) (2015) 375–406.

[35] L. Li, G. Zhang, K. Khandelwal, Topology optimization of energy absorbing structures with maximum damage constraint, Internat. J. Numer. Methods Engrg. 112 (7) (2017) 737–775.

[36] R. Alberdi, K. Khandelwal, Topology optimization of pressure dependent elastoplastic energy absorbing structures with material damage constraints, Finite Elem. Anal. Des. 133 (2017) 42–61.

[37] L. Li, G. Zhang, K. Khandelwal, Failure resistant topology optimization of structures using nonlocal elastoplastic-damage model, Struct. Multidiscip. Optim. 58 (2018) 1589–1618.
[38] M.E. Launey, R.O. Ritchie, On the fracture toughness of advanced materials, Adv. Mater. 21 (20) (2009) 2103–2110.
[39] Z. Kang, P. Liu, M. Li, Topology optimization considering fracture mechanics behaviors at specified locations, Struct. Multidiscip. Optim. 55 (5) (2017) 1847–1864.
[40] J.R. Rice, A path independent integral and the approximate analysis of strain concentration by notches and cracks, J. Appl. Mech. 35 (2) (1968) 379–386.
[41] J. Hu, S. Yao, N. Gan, Y. Xiong, X. Chen, Fracture strength topology optimization of structural specific position using a bi-directional evolutionary structural optimization method, Eng. Optim. 52 (4) (2020) 583–602.
[42] G.X. Gu, L. Dimas, Z. Qin, M.J. Buehler, Optimization of composite fracture properties: method, validation, and applications, J. Appl. Mech. 83 (7) (2016) 071006.
[43] M. Ambati, T. Gerasimov, L. De Lorenzis, A review on phase-field models of brittle fracture and a new fast hybrid formulation, Comput. Mech. 55 (2) (2015) 383–405.
[44] T.Q. Bui, X. Hu, A review of phase-field models, fundamentals and their applications to composite laminates, Eng. Fract. Mech. 248 (2021) 107705.
[45] P. Diehl, R. Lipton, T. Wick, M. Tyagi, A Comparative Review of Peridynamics and Phase-Field Models for Engineering Fracture Mechanics, engrXiv, 2021.
[46] L. Xia, D. Da, J. Yvonnet, Topology optimization for maximizing the fracture resistance of quasi-brittle composites, Comput. Methods Appl. Mech. Engrg. 332 (2018) 234–254.
[47] J.B. Russ, H. Waisman, Topology optimization for brittle fracture resistance, Comput. Methods Appl. Mech. Engrg. 347 (2019) 238–263.
[48] J.B. Russ, H. Waisman, A novel topology optimization formulation for enhancing fracture resistance with a single quasi-brittle material, Internat. J. Numer. Methods Engrg. 121 (13) (2020) 2827–2856.
[49] D. Da, J. Yvonnet, Topology optimization for maximizing the fracture resistance of periodic quasi-brittle composites structures, Materials 13 (15) (2020) 3279.
[50] C. Wu, J. Fang, S. Zhou, Z. Zhang, G. Sun, G.P. Steven, Q. Li, Level-set topology optimization for maximizing fracture resistance of brittle materials using phase-field fracture model, Internat. J. Numer. Methods Engrg. 121 (13) (2020) 2929–2945.
[51] C. Wu, J. Fang, S. Zhou, Z. Zhang, G. Sun, G.P. Steven, Q. Li, A path-dependent level set topology optimization with fracture criterion, Comput. Struct. 249 (2021) 106515.
[52] R. Jones, P. Chaperon, M. Heller, Structural optimisation with fracture strength constraints, Eng. Fract. Mech. 69 (13) (2002) 1403–1423.
[53] T. Nishioka, S. Atluri, Analytical solution for embedded elliptical cracks, and finite element alternating method for elliptical surface cracks, subjected to arbitrary loadings, Eng. Fract. Mech. 17 (3) (1983) 247–268.
[54] R. Das, R. Jones, Y. Xie, Design of structures for optimal static strength using ESO, Eng. Fail. Anal. 12 (1) (2005) 61–80.
[55] D. Kujawski, Estimations of stress intensity factors for small cracks at notches, Fatigue Fract. Eng. Mater. Struct. 14 (10) (1991) 953–965.
[56] V.J. Challis, A.P. Roberts, A.H. Wilkins, Fracture resistance via topology optimization, Struct. Multidiscip. Optim. 36 (3) (2008) 263–271.
[57] S.J. van den Boom, J. Zhang, F. van Keulen, A.M. Aragón, An interface-enriched generalized finite element method for level set-based topology optimization, Struct. Multidiscip. Optim. 63 (1) (2021) 1–20.
[58] S. Soghrati, A.M. Aragón, C.A. Duarte, P.H. Geubelle, An interface-enriched generalized FEM for problems with discontinuous gradient fields, Internat. J. Numer. Methods Engrg. 89 (8) (2012) 991–1008.
[59] M. Silva, P.H. Geubelle, D.A. Tortorelli, Energy release rate approximation for small surface-breaking cracks using the topological derivative, J. Mech. Phys. Solids 59 (5) (2011) 925–939.
[60] D.J. Payen, K.J. Bathe, A stress improvement procedure, Comput. Struct. 112–113 (2012) 311–326.
[61] R. Sharma, J. Zhang, M. Langelaar, F. van Keulen, A.M. Aragón, An improved stress recovery technique for low-order 3D finite elements, Internat. J. Numer. Methods Engrg. 114 (1) (2018) 88–103.
[62] J. Zhang, A.M. Aragón, An improved stress recovery technique for the unfitted finite element analysis of discontinuous gradient fields, Internat. J. Numer. Methods Engrg. (2021) http://dx.doi.org/10.1002/nme.6825.
[63] R. Lins, S.P. Proença, C.A. Duarte, Efficient and accurate stress recovery procedure and a posteriori error estimator for the stable generalized/extended finite element method, Internat. J. Numer. Methods Engrg. 119 (12) (2019) 1279–1306.
[64] K. Svanberg, The method of moving asymptotes—a new method for structural optimization, Internat. J. Numer. Methods Engrg. 24 (2) (1987) 359–373.
[65] A.M. Aragón, B. Liang, H. Ahmadian, S. Soghrati, On the stability and interpolating properties of the Hierarchical Interface-enriched Finite Element Method, Comput. Methods Appl. Mech. Engrg. 362 (2020) 112671.
[66] F.B. Barros, S.P.B. Proença, C.S. de Barcellos, On error estimator and p-adaptivity in the generalized finite element method, Internat. J. Numer. Methods Engrg. 60 (2004) 2373–2398.
[67] G. Zi, T. Belytschko, New crack-tip elements for XFEM and applications to cohesive cracks, Internat. J. Numer. Methods Engrg. 57 (2003) 2221–2240.
[68] S.J. van den Boom, J. Zhang, F. van Keulen, A.M. Aragón, A stable interface-enriched formulation for immersed domains with strong enforcement of essential boundary conditions, Internat. J. Numer. Methods Engrg. 120 (10) (2019) 1163–1183.
[69] J.A. Sethian, A. Wiegmann, Structural boundary design via level set and immersed interface methods, J. Comput. Phys. 163 (2) (2000) 489–528.
[70] S. Wang, M.Y. Wang, Radial basis functions and level set method for structural topology optimization, Internat. J. Numer. Methods Engrg. 65 (12) (2006) 2060–2090.

[71] H. Wendland, Piecewise polynomial, positive definite and compactly supported radial functions of minimal degree, Adv. Comput. Math. 4 (1) (1995) 389–396.

[72] J. Nocedal, S.J. Wright, Sequential quadratic programming, Numer. Optim. (2006) 529–562.

[73] E. Haber, A multilevel, level-set method for optimizing eigenvalues in shape design problems, J. Comput. Phys. 198 (2) (2004) 518–534.

[74] N. van Dijk, M. Langelaar, F. van Keulen, Explicit level-set-based topology optimization using an exact Heaviside function and consistent sensitivity analysis, Internat. J. Numer. Methods Engrg. 91 (1) (2012) 67–97.

[75] P. Liu, Y. Luo, Z. Kang, Multi-material topology optimization considering interface behavior via XFEM and level set method, Comput. Methods Appl. Mech. Engrg. 308 (2016) 113–133.

[76] M. Cui, C. Luo, G. Li, M. Pan, The parameterized level set method for structural topology optimization with shape sensitivity constraint factor, Eng. Comput. 37 (2) (2021) 855–872.

[77] J.A. Sethian, Level Set Methods and Fast Marching Methods: Evolving Interfaces in Computational Geometry, Fluid Mechanics, Computer Vision, and Materials Science, Vol. 3, Cambridge University Press, 1999.

[78] J.A. Sethian, Evolution, implementation, and application of level set and fast marching methods for advancing fronts, J. Comput. Phys. 169 (2) (2001) 503–555.

[79] M.Y. Wang, X. Wang, D. Guo, A level set method for structural topology optimization, Comput. Methods Appl. Mech. Engrg. 192 (1) (2003) 227–246.

[80] G. Allaire, F. Jouve, A.-M. Toader, Structural optimization using sensitivity analysis and a level-set method, J. Comput. Phys. 194 (1) (2004) 363–393.

[81] S. Osher, R. Fedkiw, Level Set Methods and Dynamic Implicit Surfaces, Vol. 153, Springer Science & Business Media, 2006.

[82] L. Jiang, S. Chen, Parametric structural shape & topology optimization with a variational distance-regularized level set method, Comput. Methods Appl. Mech. Engrg. 321 (2017) 316–336.

[83] M. Beghini, L. Bertini, V. Fontanari, Stress intensity factors for an inclined edge crack in a semiplane, Eng. Fract. Mech. 62 (6) (1999) 607–613.

[84] K. Alidoost, P.H. Geubelle, D.A. Tortorelli, Energy release rate approximation for edge cracks using higher-order topological derivatives, Int. J. Fract. 210 (1–2) (2018) 187–205.

[85] P. Wei, M.Y. Wang, X. Xing, A study on X-FEM in continuum structural optimization using a level set model, Comput. Aided Des. 42 (8) (2010) 708–719.

[86] N. Moës, A. Gravouil, T. Belytschko, Non-planar 3D crack growth by the extended finite element and level sets—Part I: Mechanical model, Internat. J. Numer. Methods Engrg. 53 (11) (2002) 2549–2568.

[87] M. Polajnar, F. Kosel, R. Drazumeric, Structural optimization using global stress-deviation objective function via the level-set method, Struct. Multidiscip. Optim. 55 (1) (2017) 91–104.

[88] S.H. Nguyen, H.G. Kim, Stress-constrained shape and topology optimization with the level set method using trimmed hexahedral meshes, Comput. Methods Appl. Mech. Engrg. 366 (2020) 113061.

[89] L. Van Miegroet, Generalized Shape Optimization Using XFEM and Level Set Description (Ph.D. thesis), Universit é de Li é ge, Li é ge, Belgium, 2012.

[90] L. Noël, P. Duysinx, Shape optimization of microstructural designs subject to local stress constraints within an XFEM-level set framework, Struct. Multidiscip. Optim. 55 (6) (2017) 2323–2338.

[91] O.C. Zienkiewicz, J.Z. Zhu, The superconvergent patch recovery and a posteriori error estimates. Part 1: The recovery technique, Internat. J. Numer. Methods Engrg. 33 (7) (1992) 1331–1364.

[92] K. Washizu, Variational Methods in Elasticity and Plasticity, Pergamon Press, 1982.

[93] Y. Mei, X. Wang, A level set method for structural topology optimization and its applications, Adv. Eng. Softw. 35 (7) (2004) 415–441.

[94] G. Allaire, F. De Gournay, F. Jouve, A.M. Toader, Structural optimization using topological and shape sensitivity via a level set method, Control Cybernet. 34 (1) (2005) 59.

[95] X. Guo, W. Zhang, M.Y. Wang, P. Wei, Stress-related topology optimization via level set approach, Comput. Methods Appl. Mech. Engrg. 200 (47–48) (2011) 3439–3452.

[96] M.Y. Wang, L. Li, Shape equilibrium constraint: a strategy for stress-constrained structural topology optimization, Struct. Multidiscip. Optim. 47 (3) (2013) 335–352.

[97] K. Alidoost, M. Feng, P.H. Geubelle, D.A. Tortorelli, Energy release rate approximation for small surface cracks in three-dimensional domains using the topological derivative, J. Appl. Mech. 87 (4) (2020).